

Article

Synthesis of Catalytic Ni/Cu Nanoparticles from Simulated Wastewater on Li–Al Mixed Metal Oxides for a Two-Stage Catalytic Process in Ethanol Steam Reforming: Catalytic Performance and Coke Properties

Yu-Jia Chen ¹, Song-Hui Huang ¹, Jun-Yen Uan ^{1,2,*} and Hao-Tung Lin ³

¹ Department of Materials Science and Engineering, National Chung Hsing University, 145 Xingda Rd., Taichung 40227, Taiwan; t820207@gmail.com (Y.-J.C.); d099066006@mail.nchu.edu.tw (S.-H.H.)

² Innovation and Development Center of Sustainable Agriculture (IDCSA), National Chung Hsing University, 145 Xingda Rd., Taichung 40227, Taiwan

³ Green Energy and Environment Research Laboratories, Energy Storage System Department, New Energy Technology Division, Industrial Technology Research Institute, 195, Sec. 4, Chung Hsing Rd., Chutung, Hsinchu 31040, Taiwan; haotunglin@itri.org.tw

* Correspondence: jyuan@nchu.edu.tw



Citation: Chen, Y.-J.; Huang, S.-H.; Uan, J.-Y.; Lin, H.-T. Synthesis of Catalytic Ni/Cu Nanoparticles from Simulated Wastewater on Li–Al Mixed Metal Oxides for a Two-Stage Catalytic Process in Ethanol Steam Reforming: Catalytic Performance and Coke Properties. *Catalysts* **2021**, *11*, 1124. <https://doi.org/10.3390/catal11091124>

Academic Editor: Mohamad Hassan Amin

Received: 24 August 2021

Accepted: 16 September 2021

Published: 18 September 2021

Publisher's Note: MDPI stays neutral with regard to jurisdictional claims in published maps and institutional affiliations.



Copyright: © 2021 by the authors. Licensee MDPI, Basel, Switzerland. This article is an open access article distributed under the terms and conditions of the Creative Commons Attribution (CC BY) license (<https://creativecommons.org/licenses/by/4.0/>).

Abstract: This work recovered Ni or Cu cations from simulated electroplating wastewater to synthesize Ni/Cu nano-catalysts for H₂ generation by ethanol steam reforming (ESR). Aluminum lathe waste was used as a framework to prepare the structured catalyst. Li–Al–CO₃ layered double hydroxide (LDH) was electrodeposited on the surface of the framework. The LDH was in a platelet-like structure, working as a support for the formation of the precursor of the metal catalysts. The catalytic performance and the coke properties of a 6Cu_6Ni two-stage catalyst configuration herein used for ESR catalytic reaction were studied. The Cu–Ni two-stage catalyst configuration (6Cu_6Ni) yielded more H₂ (~10%) than that by using the Ni-based catalyst (6Ni) only. The 6Cu_6Ni catalyst configuration also resulted in a relatively stable H₂ generation rate vs. time, with nearly no decline during the 5-h reaction. Through the pre-reaction of ethanol-steam mixture with Cu/LiAlO₂ catalyst, the Ni/LiAlO₂ catalyst in the 6Cu_6Ni catalyst configuration could steadily decompose acetaldehyde, and rare acetate groups, which would evolve condensed coke, were formed. The Ni nanoparticles were observed to be lifted and separated by the carbon filaments from the support and had no indication of sintering, contributing to the bare deactivation of the Ni/LiAlO₂ catalyst in 6Cu_6Ni.

Keywords: hydrogen generation; ethanol steam reforming; aluminum lathe waste; structured catalyst; layered double hydroxide; metallic nano-catalyst

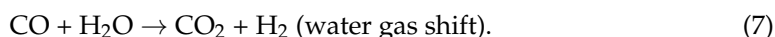
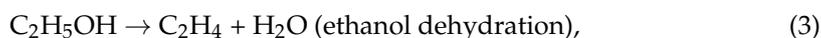
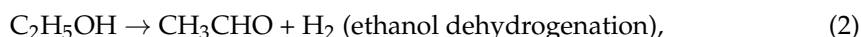
1. Introduction

Nickel plating and copper plating are often conducted in the preparation of a surface for treatment or as the final treatment of many items in everyday use [1,2]. Significant quantities of Ni and Cu cations are thus frequently present in plating wastewater. To protect public health and aquatic life, excessive quantities of Ni and Cu ions must be removed from industrial effluent before it is discharged into the public wastewater treatment system [2,3]. The authors' earlier investigation [4] reviewed numerous methods for treating nickel plating and copper plating wastewater, including filtration, membrane separation, ion-exchange, precipitation, adsorption, and biosorption. Studies concerning the extraction of Ni²⁺ and Cu²⁺ either from the electroplating wastewater or the rinse stream when plated workpieces are washed are very few. This work concerned a new process used to recover metal ions from simulated Ni or Cu electroplating wastewater for use in the synthesis of nano-catalysts. Additionally, the use of the prepared Ni- and Cu-based catalysts in ethanol steam reforming (ESR) to produce hydrogen was investigated.

Hydrogen is regarded as a promising source of energy because it is a clean fuel that combusts to produce only water [5]. Currently, methods of H₂ production include photocatalysts [6], electrolysis of water [7], metal hydrolysis [8], biomass processes [9], and steam reforming [10]. Steam reforming is the most widely used process for generating H₂ because of its high H₂ yield, low energy requirement, and low cost [5]. Ethanol is a potential feedstock for steam reforming since it is a renewable resource that can be generated in large amounts from biomass. Additionally, ethanol is not toxic, easy to handle, and has the potential to yield large amounts of H₂ [11]. The complete ESR reaction is as the following.



The main reaction paths in ESR are as follows [12].



Ni is the most widely used catalyst in the industrial production of H₂ by steam reforming due to its efficient cracking of the C–C bond and lower cost than noble metal catalysts (such as Pd, Pt, Ru, and Rh) [11]. The main challenges associated with the use of Ni-based catalysts are the formation of coke and the sintering of Ni particles, which both cause the deactivation of Ni catalysts [12]. Freni et al. [13] designed a Cu–Ni two-layer catalytic reactor to improve the catalytic performance of ESR reactions. In their experiments, ethanol/water mixture first passed through the first-layer Cu/SiO₂ catalyst, which is an effective catalyst for the dehydrogenation of ethanol to acetaldehyde (CH₃CHO), at 370 °C. The low operating temperature prevented the sintering of the Cu catalyst and reduces the formation of ethylene (C₂H₄). Then, the reacted atmosphere passed through the second-layer Ni/MgO catalyst to be further decomposed into syngas of H₂, CO₂, CO, and other gases. The relatively high operating temperature (at 650 °C) for the Ni/MgO catalyst promoted the conversion of ethanol, while the generation of some undesirable by-products, such as CO and C₂H₄, also increased. The two-layer catalytic reactor is difficult to down-size to a nano-scale structure, whose high surface area favors a complete and efficient ESR reaction. In this work, high-density distributed Ni and Cu nanoparticles were prepared on a special collocation of catalyst support (Li–Al layered double hydroxide) and substrate (aluminum lathe waste) for use in Cu–Ni two-stage catalyst configuration. The influence of a Cu-based catalyst on coke formation, nanoparticles sintering, and partial deactivation of subsequent Ni-based catalyst was investigated.

Catalyst supports can influence the nature of catalysts and even the catalytic reaction paths [12]. In some studies, layered double hydroxides (LDHs) have been applied to be catalyst supports [14]. LDHs are a series of hydrotalcite-like clays which consist of positively charged layers with intercalated water molecules and anions for charge balance. The positively charged layers are composed of mono- or di- and trivalent metal cations in hydroxyl slabs. One special case involving monovalent cations, Li–Al LDH, in which Li⁺ occupies the octahedral interstitial sites of gibbsite (Al(OH)₃) sheets to form positively charged layers, and the present authors previously studied this case [15–17]. Although several types of LDH have been studied, there is no study using Li–Al LDH as support to disperse nano-scale Ni or Cu particles on its surface. In this study, the use of Li–Al LDH as the catalyst support for Ni or Cu nano-catalysts was studied. LDHs are calcined and transferred into the so-called “mixed metal oxides” to possess the properties of high surface area, high thermal stability, high metal dispersion, and others. The calcination

product of Li–Al LDH, LiAlO_2 , has been found to have high basicity, and its basicity is even higher than that of Mg–Al LDH [18]. According to the mechanism introduced by Cosimo et al. [19], the strong basic-acid pairs on Mg–Al mixed metal oxides helped to adsorb ethanol molecules and induced the forming of acetaldehyde. The effect of LiAlO_2 on the catalytic reaction of ESR was investigated in this work.

In most relevant investigations, powdered new catalysts are investigated to obtain better performance of ESR. However, the stacking of powder in a reaction bed often causes non-uniform temperature distribution and pressure drop [20]. Processing the catalyst powder into the form of pellets is one of the solutions to reduce the pressure drop. In addition, the use of structured catalysts, such as some ceramic/metal foams and monoliths, has been investigated for resolving the issues of non-uniform temperature distribution and pressure drop in a reaction bed [20–24]. This work is the first to use aluminum lathe waste as the substrate of a structured catalyst. Aluminum lathe waste is an industrial residue generated from the processing of aluminum alloys on lathes, so that it can be recycled and reused at a relatively low cost. Metal substrates also have better thermal conductivity than ceramics, and can provide a relatively uniform temperature distribution [23,24]. To disperse catalytic nanoparticles at high density on a surface with a large area, a Li–Al– CO_3 LDH thin film was formed on the lathe waste surface using a method of electrodeposition that can be found in an earlier study by the authors, in which a Li–Al LDH coating was prepared on an Mg alloy substrate [15]. Aluminum foil and lithium hydroxide were used to prepare Al^{3+} - and Li^+ -containing solution as the electrolyte for electrodeposition [25]. Aqueous solutions of Ni or Cu ions that simulate the industrial wastewater were used as sources of Ni and Cu for the formation of metallic nanoparticles. The use of LDHs for the removal of heavy metal ions (Cu^{2+} , Cd^{2+} , Pd^{2+} , Cr^{2+} , and others) from aqueous solutions has been studied [26]. In the present study, the calcined Li–Al LDH-coated aluminum lathe waste worked as a framework for forming catalyst precursors on it, and by the way, it removed heavy metal ions when being dipped in the simulated wastewater containing Ni^{2+} or Cu^{2+} (as revealed by the experimental photographs in Figure S1). Figure S1a shows that the Ni^{2+} concentration decreased from the original 535 ppm to 3.3 ppm, as the framework immersion in the simulated wastewater. The Ni catalyst precursor was formed on the surface of the framework, leading to the reduction of Ni^{2+} in the wastewater. Similarly, Figure S1b suggests that Cu^{2+} concentration decreased from the original 78 ppm to 4.8 ppm. Herein, the removal of the metal ions from the wastewater would lead to the formation of the precursor of Ni or Cu nano-catalysts. This study investigated the microstructures of the nano-catalysts on LiAlO_2 support. Moreover, their catalytic performance in ESR was examined. The objective of this research is to combine the utility of industrial waste (lathe waste and plating wastewater) and the beneficial support properties of LDH for the synthesis of a catalyst from the perspective of the environmentally friendly process. The catalyst is synthesized on a structured substrate made of Al lathe waste to obtain good catalyst nanoparticles dispersion and adhesion on the structured support. The roles of Ni/Cu catalysts and LiAlO_2 support in ESR are clarified to explore the appreciate reaction conditions.

2. Results and Discussion

2.1. Catalyst Characteristics

Figure 1a presents the XRD pattern of the as-prepared Li–Al– CO_3 LDH that was coated on aluminum lathe waste by electrodeposition. Diffraction peaks of Li–Al– CO_3 LDH (JCPDS 42-0729), as well as those of the aluminum substrate, are observed, suggesting that the electrodeposition method deposited Li–Al– CO_3 LDH on the aluminum substrate. Figure 1b shows the XRD pattern of this coating following calcination treatment at 500 °C for 3 h. Huang et al. [27] and our previous study [17] suggested that Li–Al– CO_3 LDH transferred into mixed metal oxides with low crystallinity after it was heated at 400–500 °C. Accordingly, in Figure 1b, only two weak peaks at around 22.3° and 24.3°, corresponding to LiAlO_2 (JCPDS 75-0905), are obtained. Figure 1c displays SEM surface

morphologies of the as-prepared Li–Al–CO₃ LDH coating on aluminum lathe waste. Li–Al–CO₃ LDH had vertical platelet-like structures and densely covers the surface of the aluminum substrate. Calcination at 500 °C for 3 h did not change the surface morphology of the coating, but it slightly distorted the platelets (as shown in Figure 1d). The results in Figure 1d proved that the nano-structured catalyst support was not destroyed during high-temperature calcination.

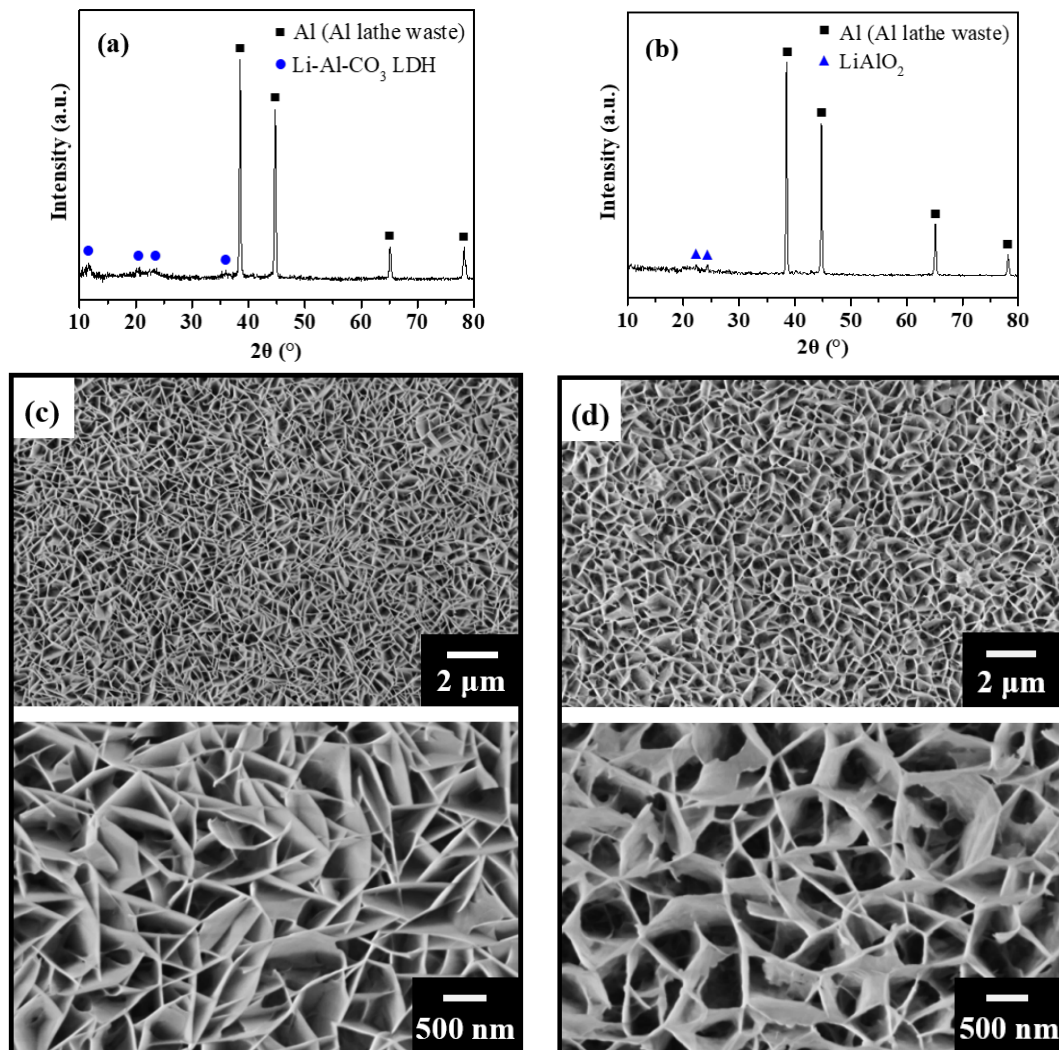


Figure 1. GAXRD patterns of: (a) Li–Al–CO₃ LDH coating on aluminum lathe waste by electrodeposition; (b) the coated material after calcination at 500 °C for 3 h. SEM surface morphologies of: (c) Li–Al–CO₃ LDH coating on aluminum lathe waste by electrodeposition; (d) the coated material after calcination at 500 °C.

The basicity and acidity properties of the LiAlO₂ support were studied by temperature programmed desorption (TPD). Figure 2a,b present TPD-CO₂ and TPD-NH₃ profiles of the LiAlO₂ support, respectively. The CO₂ desorption curve (shown in Figure 2a) reveals the basicity property of the sample. In Figure 2a, a small peak appears at a low temperature of 115 °C, corresponding to the weak Brønsted basic sites (–OH). At 200–400 °C, the strong peak represents that CO₂ was desorbed from the moderate Lewis basic sites (Li⁺–O^{2–} pairs). At high temperature range (400–600 °C), a minor peak indicates the strong basic sites (isolated O^{2–}) [18]. The NH₃ desorption curve shown in Figure 2b, on the other hand, reveals the acidity property of the sample. In Figure 2b, the desorption curve of NH₃ presents three peaks corresponding to the weak (100–200 °C), medium (200–400 °C), and

strong (400–600 °C) acid sites. They are mainly associated with the absorption of NH_3 by Lewis acid sites ($\text{Al}^{3+}-\text{O}^{2-}$ pairs) with various strengths [28].

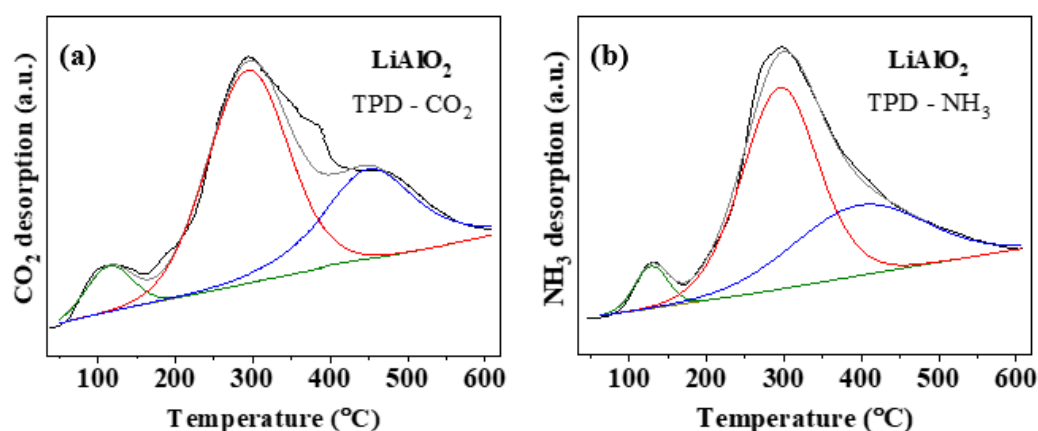


Figure 2. (a) TPD- CO_2 ; (b) TPD- NH_3 profiles of the LiAlO_2 support.

Table 1 presents the fractions of different sites (weak, medium, and strong sites) of the total number of CO_2/NH_3 desorption sites on LiAlO_2 according to the TPD profiles. As revealed in Table 1, the medium basic/acidic sites account for the largest proportion of the total number of basic/acidic sites, with fractions of ~60%. The total number of basic sites is greater than the total number of acid sites, and the ratio of the two is 1.44. Choong et al. [28] added various amounts of Ca onto Al_2O_3 ; the ratio of basic/acidic sites increased with the amounts of Ca addition. Their experimental results confirmed that the appreciated amounts of Ca addition could suppress the ethanol dehydration reaction (Equation (3)) and reduce the formation of ethylene in ESR compared with the result of pure Al_2O_3 . The performance of LiAlO_2 support in ethanol decomposition is discussed in the following Section 2.2.

Table 1. The fractions of different sites (weak, medium, and strong sites) of the total number of CO_2/NH_3 desorption sites on LiAlO_2 according to the TPD profiles.

Site	CO_2 Desorption	NH_3 Desorption
Weak (%)	7.32	5.29
Medium (%)	60.98	59.47
Strong (%)	31.71	35.24
B/A ^a	1.44 ^a	

^a Total number of basic sites (B) over total number of acid sites (A), based on the ratio of the total area of peaks of TPD- CO_2 and TPD- NH_3 .

Figure 3 presents XRD patterns and the SEM surface morphologies of the reduced catalysts (the catalyst after reduction reaction in H_2 atmosphere at 500 °C). The XRD pattern of Ni/LiAlO_2 (Figure 3a) includes a broad, weak characteristic peak of Ni (200) at 51.9° . The characteristic peak of Ni (111) is very close to that of Al (111) at 44.5° and is therefore difficult to distinguish. The broad and weak peaks are considered to arise from tiny particles with high dispersion [29]. The XRD pattern of Cu/LiAlO_2 (Figure 3b) includes peaks of Cu (at 43.3° , 50.5° , and 74.1°) and Cu_2O (at 36.4° , 46.3° , and 73.6°). The SEM surface morphologies of the Ni/LiAlO_2 catalyst in Figure 3c show nanoparticles (~10 nm in size) at high density on the surface of LiAlO_2 platelets. In contrast, concerning the Cu/LiAlO_2 catalyst, shown in Figure 3d, the particles on the LiAlO_2 platelets are sparsely distributed. The sizes of the particles on the Cu/LiAlO_2 catalyst varied significantly. The larger particles had diameters of about 100 nm while some of the tiny particles had diameters of about 10 nm.

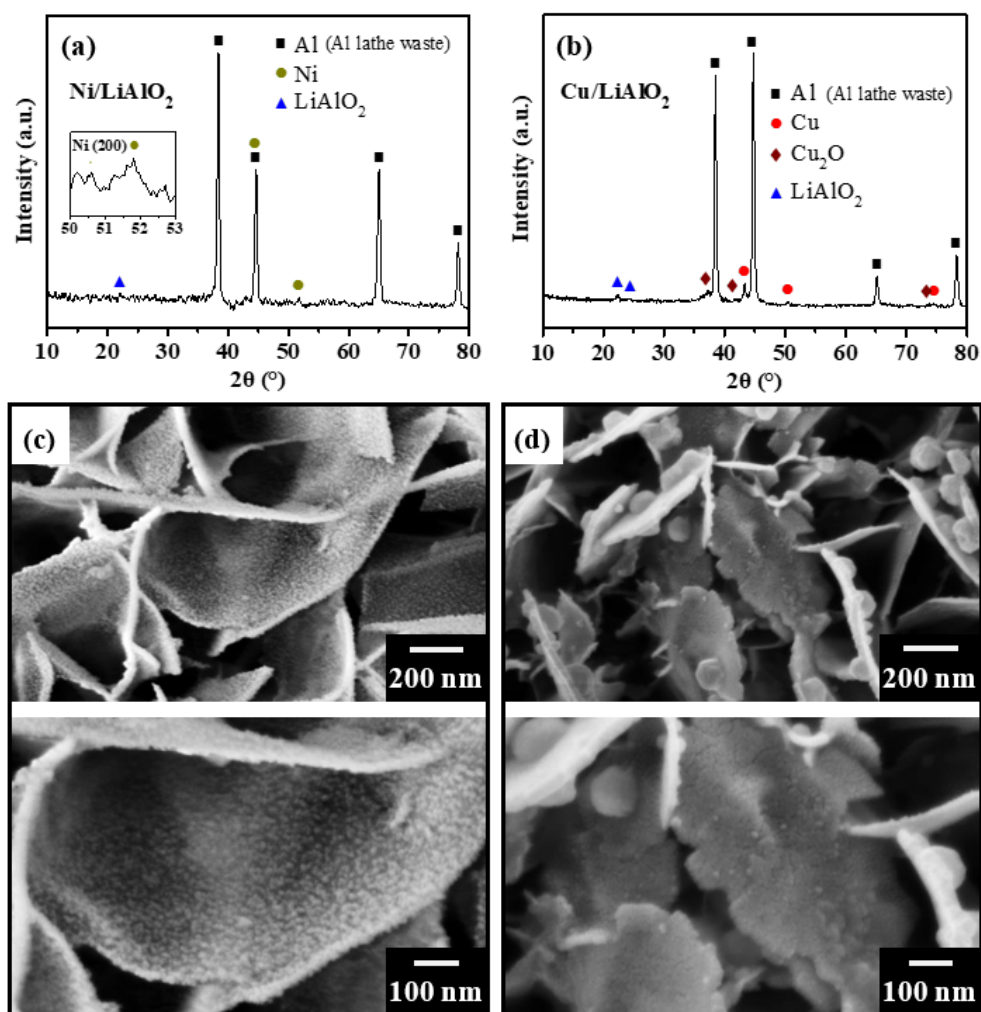


Figure 3. GAXRD patterns of the reduced catalysts obtained herein: (a) Ni/LiAlO₂; (b) Cu/LiAlO₂. SEM surface morphologies of the reduced catalysts obtained herein: (c) Ni/LiAlO₂; (d) Cu/LiAlO₂.

Figure 4 presents TEM cross-sectional images of the Ni/LiAlO₂ catalyst. As shown in Figure 4a, nanoparticles were densely and uniformly distributed on the LiAlO₂ platelets. The corresponding TEM dark field image (Figure 4b) shows bright nanoparticles. Figure 4c magnifies the particles in Figure 4a, which have sizes of around 10 nm. Figure 4d shows the diffraction ring pattern of the selected area in Figure 4c. As shown in Figure 4d, the rings in the diffraction pattern are consistent with the diffraction data for Ni and NiO, suggesting that the nano-sized particles comprised Ni and NiO. Figure 5 presents TEM cross-sectional images of the Cu/LiAlO₂ catalyst. The bright-field image (Figure 5a) shows nanoparticles (~less than 20 nm in size) on LiAlO₂ platelets. The corresponding dark field image (Figure 5b) shows bright particles with sizes of ~less than 20 nm. Figure 5c magnifies the particle that is enclosed by the red dotted circle in Figure 5a, revealing crystal twinning. Figure 5d displays the diffraction pattern for this particle (the particle shown in Figure 5c). This pattern is associated with the diffraction plane (011) of Cu. The points in the diffraction pattern lie on lines, confirming the crystal twinning structure. Figure 5e presents the selected area diffraction pattern from the area within the blue dotted circle in Figure 5a. The indexing of the diffraction rings reveals polycrystalline Cu and Cu₂O in this area. From the above observations, Cu and Cu₂O nanoparticles are inferred to have formed on the Cu/LiAlO₂ catalyst, despite the presence of the agglomerates that are seen in the SEM images (Figure 3d).

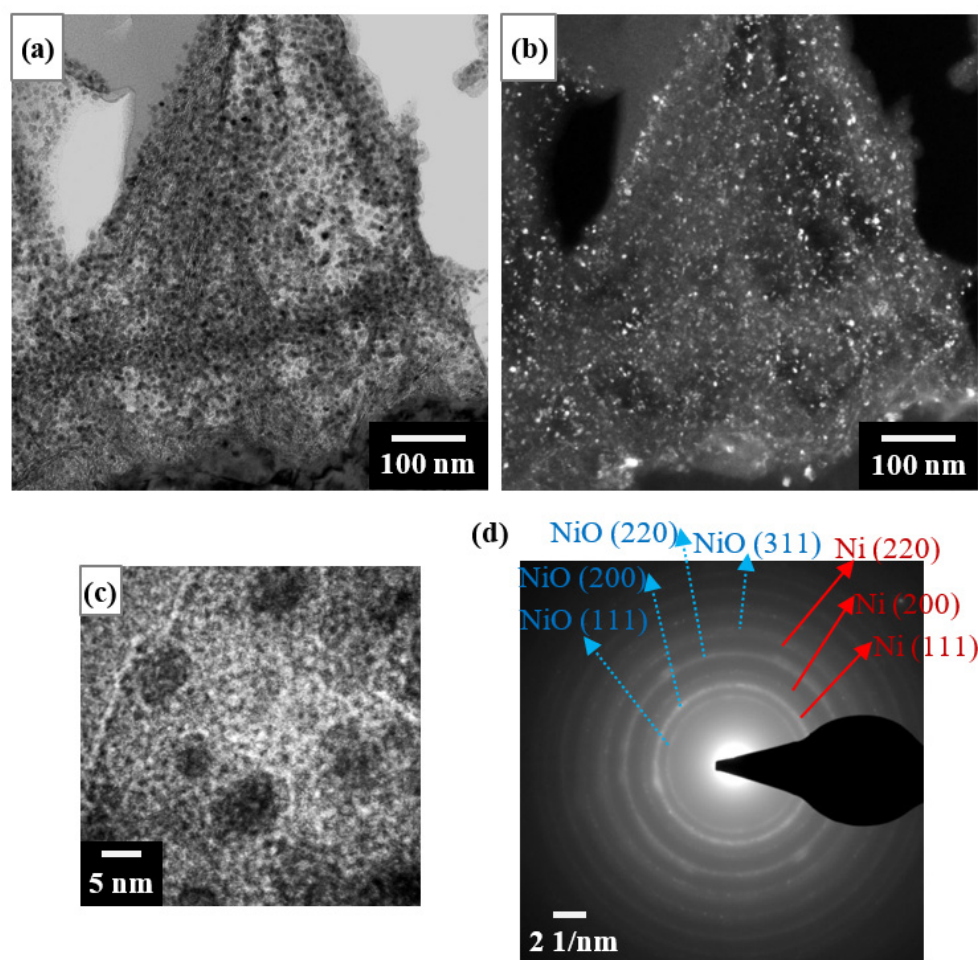


Figure 4. TEM cross-sectional observations of the Ni/LiAlO₂ catalyst: (a) bright-field image; (b) dark-field image; (c) magnified view of particles in Figure 4a; (d) selected area diffraction pattern of the particles.

Figure 6 displays XPS spectra of the reduced catalysts. The XPS examination of Ni/LiAlO₂ focuses on Ni 2p_{3/2} to identify the states of Ni (Figure 6a). As shown in Figure 6a, besides the surface data (the upper curve), the subsurface data (sputtering for 20 s) are also collected (shown as the bottom curve) for comparison. The binding energy of Ni⁰ is about 852.6 eV and that of Ni²⁺ is around 855.2 eV [30,31]. Another peak at around 861.3 eV corresponds to a satellite peak of Ni²⁺. The dominance of Ni²⁺ rather than Ni⁰ in the Ni 2p_{3/2} peak may be attributed to the high oxygen affinity of the high surface area of the small metal particles [32,33]. Compared with the surface data, the subsurface data present a more distinct peak corresponding to Ni⁰, which also implies that the surface of Ni nanoparticles is prone to oxidation. The Cu 2p spectrum of Cu/LiAlO₂ (Figure 6b) includes main peaks at 932.2 eV and 952.0 eV, corresponding to 2p_{3/2} and 2p_{1/2} of Cu⁰/Cu⁺, respectively [34,35]. The absence of a Cu²⁺ satellite peak between 940 eV and 950 eV suggests the absence of Cu²⁺. The characteristic peaks of Cu⁰ 2p and Cu⁺ 2p in the Cu 2p spectrum are too close to each other to allow them to be distinguished. The Auger electron spectrum (AES) of Cu LMM is examined to distinguish between Cu⁺ and Cu⁰ species on the Cu/LiAlO₂ catalyst. As shown in Figure 6c, Cu⁰ and Cu⁺ yield peaks at the binding energy of 569.9 eV and 571.8 eV, respectively. Cu⁺ accounts for a high proportion (62.7%) of the total number of Cu⁰ and Cu⁺ species, revealing that the dispersal of Cu⁺ on the surface of Cu/LiAlO₂ catalyst is higher than that of Cu⁰. The incorporation of copper into the LDH-based precursor makes the strong interaction with the oxygen of some Cu species, which would remain as Cu₂O after H₂ reduction [36]. Table 2 presents the surface

elemental composition of the reduced samples examined by XPS. According to Table 2, the catalytic metal loadings on the Ni/LiAlO₂ and Cu/LiAlO₂ catalysts are 17.5 at.% Ni and 12.3 at.% Cu, respectively.

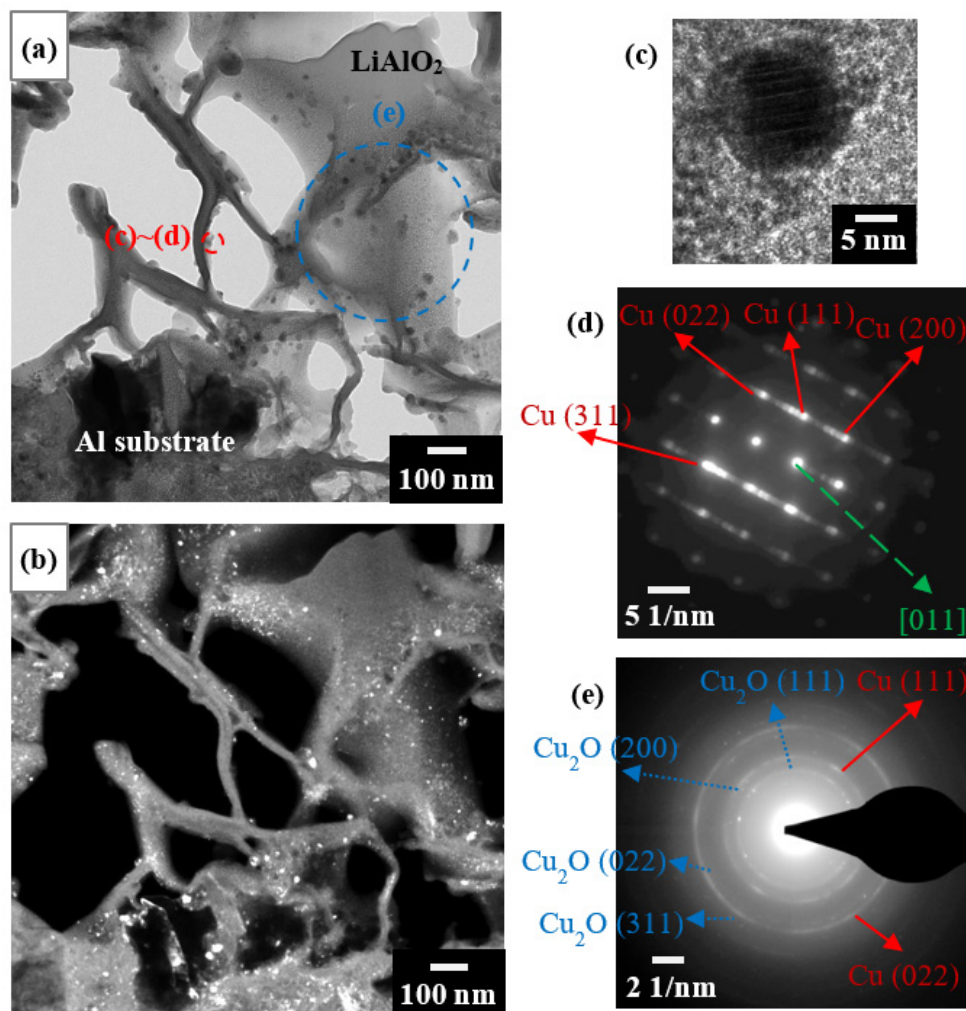


Figure 5. TEM cross-sectional observations of the Cu/LiAlO₂ catalyst: (a) bright-field image; (b) dark-field image; (c) magnified view of the particle framed by the red dotted line in Figure 5a. Selected area diffraction patterns of: (d) the particle framed by the red dotted line in Figure 5a; (e) the area framed by the blue dotted line in Figure 5a.

Table 2. Surface elemental composition of the reduced catalysts as determined by XPS.

Catalyst	XPS Compositions			
	O (at.%)	Al (at.%)	Ni (at.%)	Cu (at.%)
Ni/LiAlO ₂	68.7	13.7	17.5	–
Cu/LiAlO ₂	71.8	16.0	–	12.3

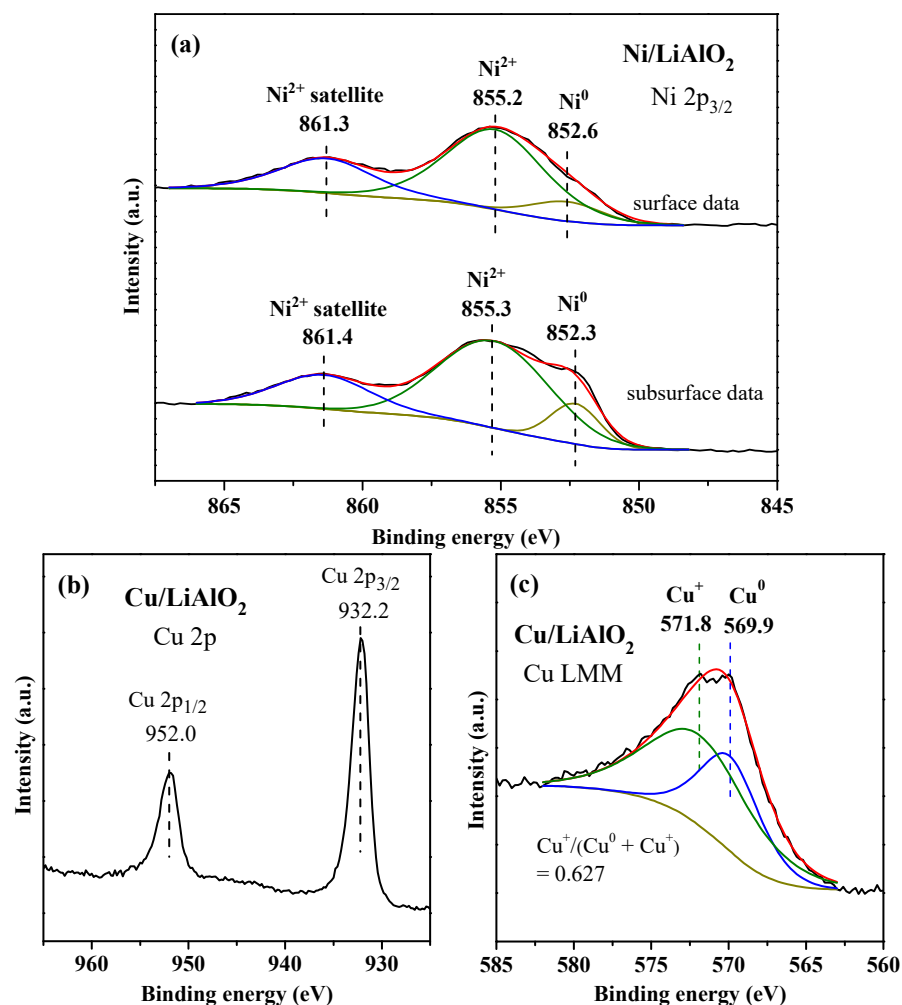


Figure 6. XPS surface spectra of the reduced catalysts obtained herein: (a) Ni $2p_{3/2}$ of Ni/LiAlO₂, the surface data is compared with the subsurface data (sputtering for 20 s); (b) Cu 2p of Cu/LiAlO₂; (c) Cu LMM AES spectrum of Cu/LiAlO₂.

2.2. Effect of LiAlO₂ Support and Cu/Ni Catalysts

Figure 7 plots the ethanol conversion (X_{EtOH}) and yields of gas-phase products in ESR over various catalyst configurations at 500 °C. The catalyst configuration with six aluminum lathe waste strip balls with LiAlO₂ on the strip surface (denoted as 6LiAlO₂), was tested to determine the effect of the LiAlO₂ support on ESR. As shown in Figure 7, 6LiAlO₂ exhibits a low ethanol conversion of 25% and provides a very low H₂ yield of ~0.2%. The 6Cu catalyst configuration provides a higher ethanol conversion of 75% and a higher H₂ yield of ~2.3% than 6LiAlO₂. No ethylene was detected in the gas generated in ESR over either catalyst configuration (as revealed by the GC-MS results in Figure S2), indicating that no ethanol dehydration (Equation (3)) occurred. The condensed liquid phase products were mainly water, ethanol, and acetaldehyde over either catalyst configuration (as revealed by the GC-MS results in Figure S3). The most acetaldehyde was obtained using 6Cu, followed by 6LiAlO₂; the last one was obtained using 6Ni or 6Cu_6Ni (which provided similar amounts). The evolution of acetaldehyde is elucidated as follows. First, the base-acid pairs on the LiAlO₂ support could provide sites for the initial adsorption of the hydroxyl group (–OH) of ethanol and the relatively large amounts of basic sites (as revealed in Table 1) could prevent the formation of ethylene, leaving a small amount of acetaldehyde as the primary product of ethanol decomposition [19,28]. Secondly, the introduction of Cu/Cu₂O onto LiAlO₂ could further improve the efficiency of ethanol dehydrogenation (Equation (2)), resulting in the Cu/LiAlO₂ generating almost twice the amount of acetaldehyde as the LiAlO₂

(according to the GC-MS results in Figure S3). Copper is known to be an effective catalyst of ethanol dehydrogenation (Equation (2)) [11]. The participation of Cu_2O in ethanol dehydrogenation (Equation (2)) has also been examined [37]. Sato et al. [38] suggested that the Cu^+/Cu^0 pairs on a Cu-based catalyst (Cu/SiO_2) exhibited high selectivity toward acetaldehyde in ethanol conversion reaction. Herein, Figure 7 shows that the 6Ni and 6Cu_6Ni catalyst configurations yield large amounts of H_2 and C1 gases (CO_2 , CO , and CH_4) because of the efficient C–C bond-breaking ability of nickel.

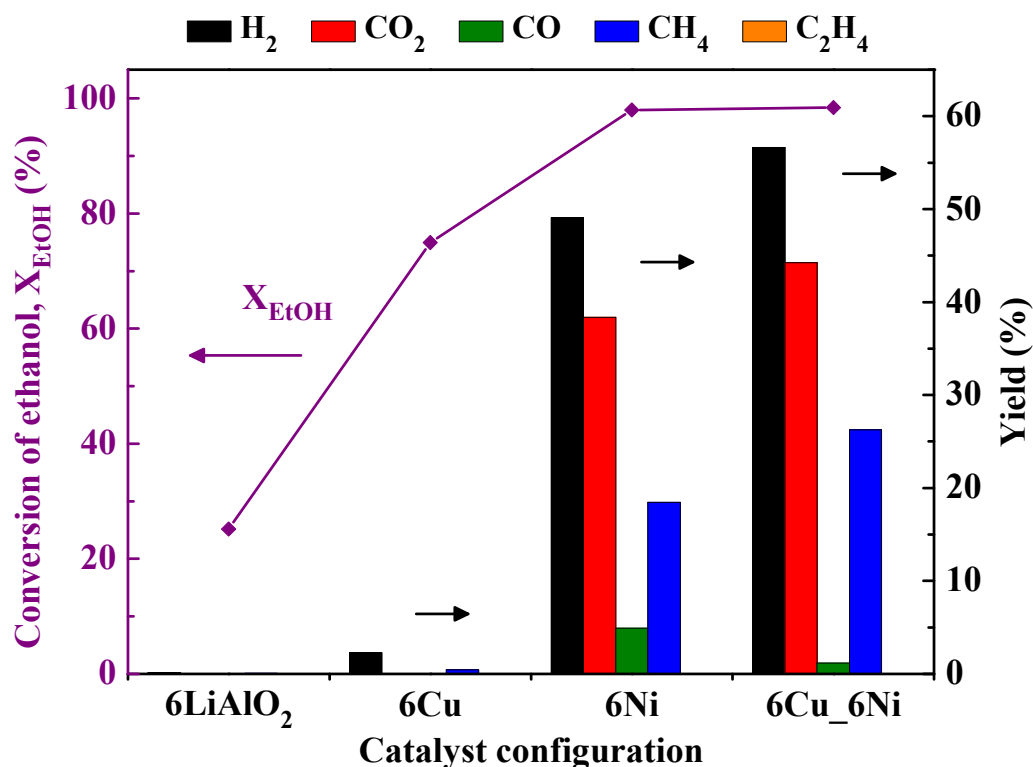


Figure 7. Ethanol conversion (X_{EtOH}) and yields of gas-phase products in ESR over various catalyst configurations. Ethanol aqueous solution with a feed rate of 0.5 mL/min was vaporized and mixed with N_2 flow for a total gas feed rate of 1000 mL/min. Reaction conditions: temperature = 500 °C; steam/ethanol (S/E) molar ratio = 10.

2.3. Effect of Temperature on ESR over 6Ni Catalyst Configuration

Figure 8 presents the effect of temperature on ethanol conversion (X_{EtOH}) and gas yields in ESR by using the 6Ni catalyst configuration. As shown in Figure 8, the ethanol conversion is higher than 95% at 400 °C, increasing gradually with temperature to 100% at 550 °C. The H_2 yield increases linearly from 15% to 60% as the temperature rises from 400 °C to 550 °C. The CO_2 yield is very low at 400 °C, revealing that the water gas shift (Equation (7)) hardly occurs. As the temperature increases to 450 °C, the amount of CO generated decreases while the amount of CO_2 generated increases to almost the amount of CH_4 generated. The almost equal amounts of CH_4 and $\text{CO}_2 + \text{CO}$ imply that acetaldehyde decomposition (Equation (4)) remains the dominant reaction that generates CO and CH_4 at 450 °C. Most of the CO is then converted to CO_2 via water gas shift (Equation (7)). As the temperature rises from 450 °C to 550 °C, the CO_2 yield continues to increase while the CH_4 yield decreases. This result reveals that acetaldehyde steam reforming (Equation (5)), methane steam reforming (Equation (6)), and water gas shift (Equation (7)) reactions are gradually enhanced. Increasing the temperature promotes these reactions, resulting in more H_2 generation.

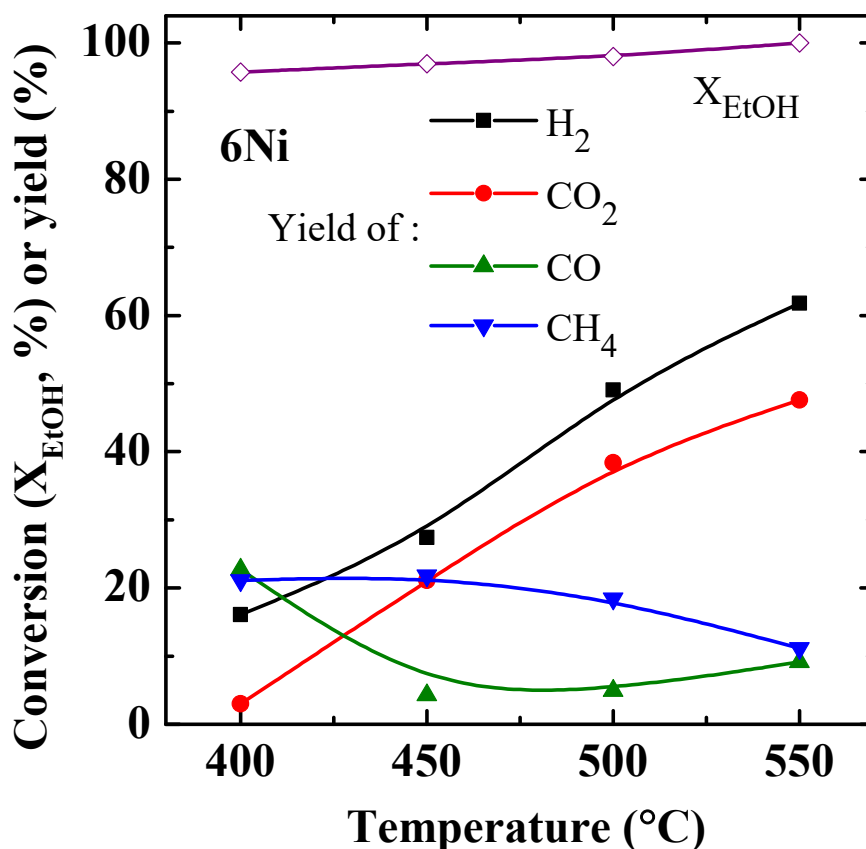


Figure 8. Effect of temperature on ethanol conversion (X_{EtOH}) and gas yields in ESR over the 6Ni catalyst configuration at a reaction time of 1 h. Reaction conditions: S/E = 10; space time = $3.42 \text{ g}_{\text{catal.}} \cdot \text{min} / \text{g}_{\text{EtOH}}$.

2.4. Effect of Temperature on ESR over 6Cu_6Ni Catalyst Configuration

Figure 9 shows the effect of temperature on ethanol conversion (X_{EtOH}) and gas yields in ESR over 6Cu_6Ni. The ethanol conversion is more than 98% above 400 °C and attains 100% at 550 °C. The H₂ yield increases almost linearly with temperature from 350 °C to 550 °C. Compared with the 6Ni catalyst configuration, the ethanol-water mixture steam feed firstly reacted with the Cu-based catalyst in 6Cu_6Ni configuration; the reacted gas then immediately passed through the Ni-based catalyst, resulting in ~10% higher H₂ yield than that of 6Ni at each temperature. As shown in Figure 9, at relatively low temperatures from 350 °C to 450 °C, more amounts CH₄ than CO₂ + CO are generated, indicating that the acetaldehyde decomposition (Equation (4)) dominates the conversion of acetaldehyde at such temperatures. Methanation (the reverse reaction of Equation (6)) converts some CO to CH₄, causing more CH₄ than CO₂ + CO to be generated. The 6Cu_6Ni catalyst configuration generates more C1 gases than the 6Ni catalyst configuration at temperatures higher than 400 °C, which proves that the decomposition of acetaldehyde is more promoted by 6Cu_6Ni. The pre-reaction of ethanol on the Cu-based catalyst facilitates the dehydrogenation steps, generating acetaldehyde and promotes the subsequent C–C bond breakage during the subsequent interaction with the Ni-based catalyst. At temperatures above 450 °C, the gas-phase distribution of 6Cu_6Ni varies similarly to that of 6Ni. Compared with 6Ni, the yields of CO₂ and CH₄ are higher and the yield of CO is lower for 6Cu_6Ni at 500 °C. It indicates that the water gas shift (Equation (7)) and methanation (the reverse reaction of Equation (6)) reactions are more promoted on 6Cu_6Ni than on 6Ni at 500 °C. The enhancement of both reactions reduces the generation of CO.

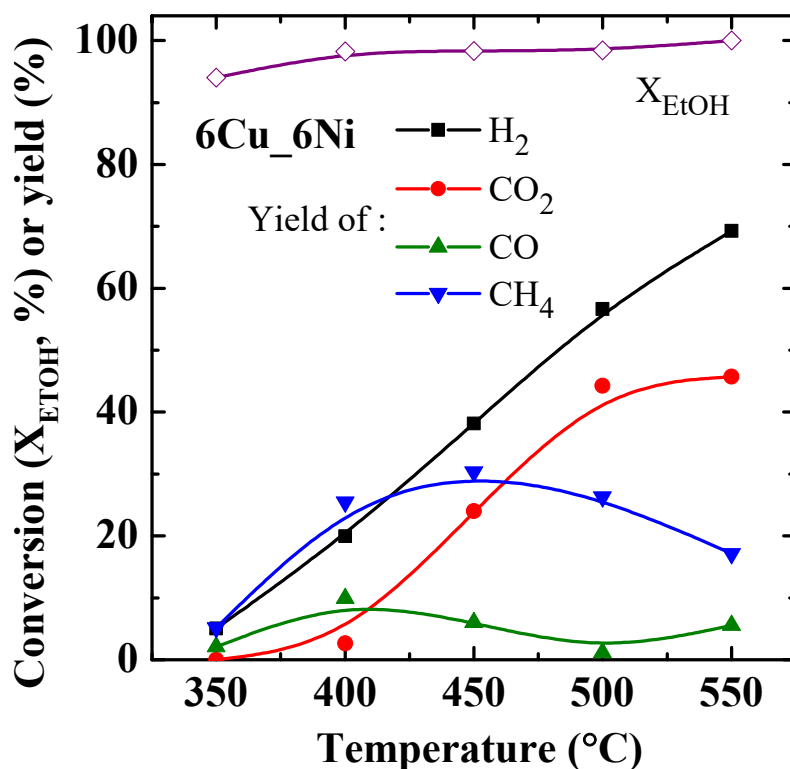


Figure 9. Effect of temperature on ethanol conversion (X_{EtOH}) and gas yields in ESR over the 6Cu_6Ni catalyst configuration at a reaction time of 1 h. Reaction conditions: S/E = 10; space time = $3.42 \text{ g}_{catal.} \cdot \text{min} / \text{g}_{EtOH}$ (space time is only based on the weight of Ni/LiAlO₂ catalyst, which is the same as that of 6Ni).

2.5. ESR vs. Reaction Time

Figure 10a plots the ethanol conversion and yields of the produced gases during prolonged reaction time over 6Ni. Ethanol conversion is 98% at 1 h, reaching 100% at 3 h, and remaining 100% until the end of the 5-h test. The H_2 yield drops from an initial 50% to 35% after 150 min; this yield is maintained until the end of the test. Yields of C1 gases also decrease as the reaction time increases, revealing catalyst partial deactivation. Figure 10b displays the performance of 6Cu_6Ni. Ethanol conversion is 99% at 1 h, which slightly exceeds that for the 6Ni catalyst at the same time. It reaches 100% at 3 h and remains at 100% until the end of the 5-h test. The yield of H_2 is approximately 57% throughout the 5-h test, showing better stability in the amounts of H_2 generation than that via the 6Ni catalyst configuration (as shown in Figure 10a). Moreover, as indicated in Figure 10b, yields of C1 gases also remain stable throughout the test, implying that the partial deactivation of the 6Cu_6Ni catalyst configuration is insignificant. Table 3 compares the H_2 yields and gas compositions that are achieved using the 6Ni and 6Cu_6Ni catalyst configurations herein and the data taken from previous studies that involve various catalysts [21–23,39–43]. As shown in the table, although test conditions are different from various studies, the experimental conditions of this study are more stringent than those used in other studies. Herein, this study employed smaller space-time conditions than those used in the various previous studies. A smaller space time can be interpreted as using a less catalyst/ethanol feed ratio for the reaction. As shown in Table 3, 6Cu_6Ni has almost the best H_2 yield among the compared structured catalysts. This yield is only lower than that obtained using Cu–Ni–K/Mg–Al LDH powder in a previous study [39] in which the catalyst was tested at a relatively high space time ($14.22 \text{ g}_{catal.} \cdot \text{min} / \text{g}_{EtOH}$) and a high background pressure of 101 kPa. Our study herein by 6Cu_6Ni had space time only $3.42 \text{ g}_{catal.} \cdot \text{min} / \text{g}_{EtOH}$. More importantly, 6Cu_6Ni also generated a relatively high H_2 yield and the lowest CO concentration, about 0.48%, than that obtained in other studies using Ni–Cu bimetal

catalysts in ESR (mostly more than 2%). CO is a pollutant of Pt catalysts that are used in fuel cells and causes them to fail. According to Devrim et al. [44], the suppression of CO in feed gas reduced the loss of current density in high-temperature proton exchange membrane fuel cells (HT-PEMFCs) and helped to maintain their performance.

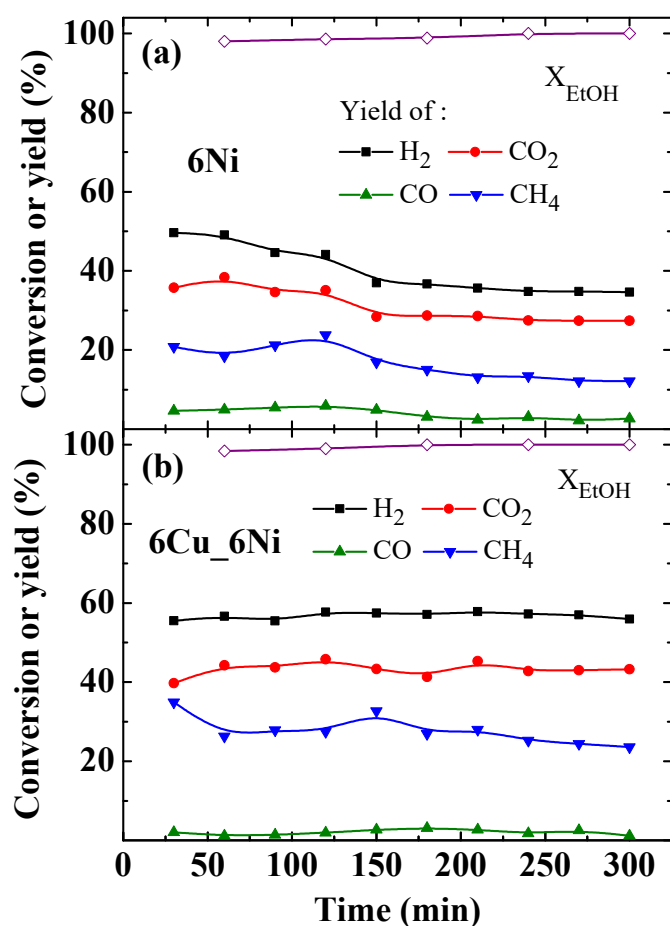


Figure 10. Ethanol conversion (X_{EtOH}) and gas yields vs. reaction time over: (a) 6Ni; (b) 6Cu_6Ni catalyst configurations. Reaction conditions: temperature = 500 °C; S/E = 10; space time = 3.42 $g_{catal.} \cdot min / g_{EtOH}$.

Table 3. Comparison of H₂ yield and gas composition in ESR over various catalysts at 500 °C.

Catalyst	Reaction Conditions		H ₂ Yield (%)	Gas Composition (vol.%)				Ref.
	S/E	Space Time ($g_{catal.} \cdot min / g_{EtOH}$)		H ₂	CO ₂	CO	CH ₄	
6Ni ^{a,b}	10	3.42	49.07	69.72	17.37	2.51	10.40	This work
6Cu_6Ni ^{a,b}	10	3.42	56.63	70.32	18.32	0.48	10.88	This work
Rh-Pd/CeO ₂ ^{b,d}	6	10.04	~33	~53	~24	~3	~20	[21]
Pt-Ni/CeO ₂ -ZrO ₂ ^{b,d}	3	6.39	~46	~60	~21	~6	~13	[22]
Ni/CeO ₂ -MgO ^b	6	101.13	~53	~62	~23	~3	~12	[23]
K-Cu-Ni/Mg-Al LDH ^{c,d}	10	14.22	~67	~67	~21	~2	~10	[39]
Cu-Ni/YSZ ^{c,d}	3	8.15	~37	~61	~18	~8	~13	[40]
Cu-Ni@Ca-SiO ₂ ^{c,d}	6	8.33	– ^e	~70	~15	~7	~8	[41]
Cu-Ni/CeO ₂ ^{c,d}	6	11.19	– ^e	~69	~18	~2	~11	[42]
Cu-Ni/Zeolite ^{c,d}	8	8.16	– ^e	~71	~20	~3	~6	[43]

^a 6Ni (i.e., Ni/LiAlO₂) and 6Cu_6Ni (i.e., Cu/LiAlO₂_Ni/LiAlO₂) catalyst configurations at reaction time of 1 h. Reaction conditions: steam/ethanol (S/E) molar ratio, S/E = 10; space time = 3.42 $g_{catal.} \cdot min / g_{EtOH}$, where $g_{catal.}$ and g_{EtOH} are the weight used for reaction.

^b Structured catalysts. ^c Powdered catalysts. ^d Bimetal catalysts. ^e Not given.

2.6. Coke Properties

The material characterization results of the spent Cu/LiAlO₂ catalyst that was used in the 5-h reaction over 6Cu_6Ni are displayed in Figure S4. The XRD pattern (Figure S4a) from the spent Cu/LiAlO₂ catalyst includes original peaks of Cu, Cu₂O, and aluminum substrate. SEM observations (Figure S4b) reveal no carbon deposition on the surface of the catalyst and no obvious sintering of Cu/Cu₂O particles. These results are consistent with studies that have noted that copper has a relatively weak effect on the cleavage of C–C bonds so the Cu/LiAlO₂ catalyst produces almost no coke [32].

Figure 11a,b presents the SEM surface images of the spent Ni/LiAlO₂ catalysts that were used in the 5-h reactions over 6Ni and 6Cu_6Ni catalyst configurations (herein denoted as Ni/LiAlO₂@6Ni and Ni/LiAlO₂@6Cu_6Ni, respectively). The coke formed on the spent Ni/LiAlO₂@6Ni (Figure 11a), exhibiting coarse- and thick-diameter filamentous coke, appears to cover the surface of the catalyst. On the other hand, the coke formed on the spent Ni/LiAlO₂@6Cu_6Ni was illustrated in Figure 11b, exhibiting filamentous coke (~20 nm in diameter) with the possible catalyst particles (the bright particles of size ~10 nm) on the top end of the filamentous coke. TEM cross-sectional observations (Figure 11c,d) reveal the nanoparticles and coke on the spent Ni/LiAlO₂ catalysts. In Figure 11c, the carbon that formed on the spent Ni/LiAlO₂@6Ni has a foam-like appearance, covering LiAlO₂ platelets and Ni nanoparticles. As shown in the high-resolution TEM image (the inserted image in Figure 11c), it seems that the particles came across other particles and caused sintering. In contrast, the spent Ni/LiAlO₂@6Cu_6Ni, as shown in Figure 11d, exhibits carbon filaments with a diameter of approximately 20 nm. Particles on the spent Ni/LiAlO₂@6Cu_6Ni, unlike the spent Ni/LiAlO₂@6Ni, are of a size similar to that of the original particles (as shown in the inserted TEM image in Figure 11d). The growth of carbon filaments lifted and separated the Ni particles, preventing them from sintering. Selected area diffraction patterns of the particles on the spent Ni/LiAlO₂@6Ni and Ni/LiAlO₂@6Cu_6Ni (shown in Figure S5a,b, respectively) suggest that these particles contain Ni and NiO.

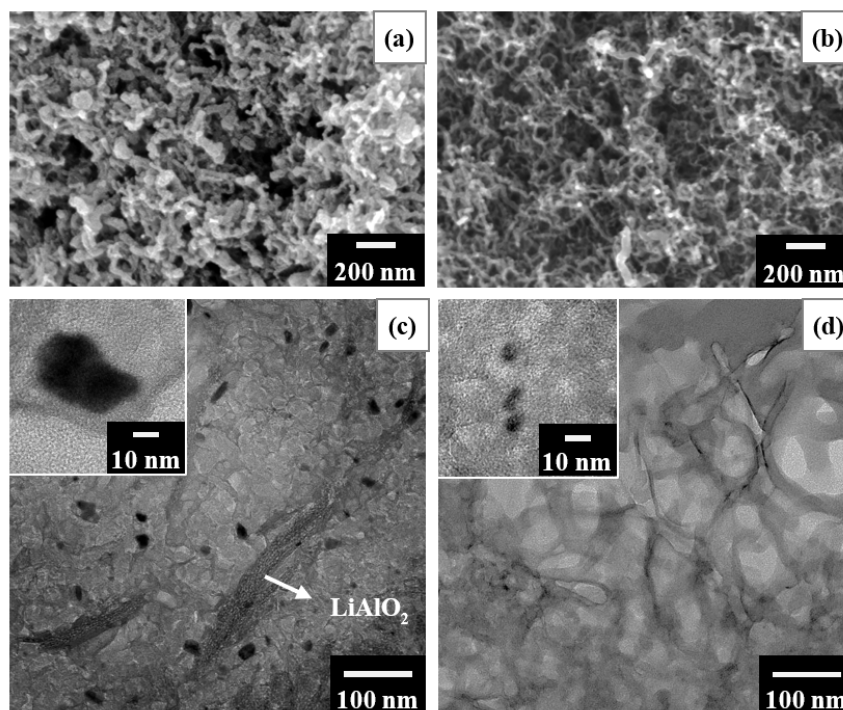


Figure 11. SEM surface morphologies of the spent catalysts that were used in 5-h reactions of ESR: (a) Ni/LiAlO₂@6Ni; (b) Ni/LiAlO₂@6Cu_6Ni. TEM cross-sectional images of the spent catalysts that were used in 5-h reactions of ESR: (c) Ni/LiAlO₂@6Ni; (d) Ni/LiAlO₂@6Cu_6Ni. Reaction conditions: same as that described in Figure 10.

Owing to the different morphologies of the carbon on the spent Ni/LiAlO₂ catalysts that were respectively used in the two different catalyst configurations, FTIR and Raman spectroscopy, were used to examine the carbon. Figure 12a shows the FTIR spectra of the coke on Ni/LiAlO₂@6Ni and Ni/LiAlO₂@6Cu_6Ni around the wavenumber of 900–1800 cm⁻¹. The absorbance bands in Figure 12a and their positions are identified and mainly correspond to the following [45–47]: 1060 cm⁻¹ for the stretching vibrational mode of C–O bonds; 1385 cm⁻¹ for the symmetric stretching vibrations of –CH₃ groups; 1440 cm⁻¹ for the symmetric bending vibrations of O=C–O bonds in acetate groups (CH₃COO–); 1540 cm⁻¹ for the C=C bonds in polycondensed aromatics; and 1640 cm⁻¹ for the C=O stretching vibrations in acetyl groups (CH₃CO–). The relative fractions of the peak area of the absorbance bands in each FTIR spectrum were displayed in Figure 12b. From Figure 12b, the band related to C=O of acetyl groups at 1640 cm⁻¹ has the nearly same fraction (about 27–29%) for the spent Ni/LiAlO₂@6Ni and Ni/LiAlO₂@6Cu_6Ni, confirming that the adsorption of acetaldehyde on the Ni/LiAlO₂ in either of the two catalyst configurations was similar. The bands at 1540 cm⁻¹ (C=C) and 1440 cm⁻¹ (OCO) show higher area fraction in the coke formed on the spent Ni/LiAlO₂@6Ni than those on the spent Ni/LiAlO₂@6Cu_6Ni. These two bands are associated with polycondensed coke, which grows simultaneously with the accumulation of acetate groups [46,47]. This non-filamentous coke could cover the Ni nanoparticles, as observed in the TEM images in Figure 11c, possibly causing the decay of the catalytic performance of the Ni/LiAlO₂@6Ni. On the other hand, the band at 1060 cm⁻¹ (C–O) accounts for a higher fraction (of ~44.7%) of peak area intensity for the coke formed on the spent Ni/LiAlO₂@6Cu_6Ni than that of Ni/LiAlO₂@6Ni (~23.5%). This reveals that the decomposition of acetaldehyde (to form CH₄ and CO) was relatively boosted by the Ni/LiAlO₂@6Cu_6Ni. Montero et al. [46] studied the coke evolution during the stages of non-deactivation and deactivation of a Ni/La₂O₃–αAl₂O₃ catalyst in ethanol steam reforming. According to Montero et al. [46], under the stage of non-deactivation state, FTIR spectrum from the surface of the catalyst showed that the area fraction corresponding to the band at ~1106 cm⁻¹ (C–O) was ~47%. The area fraction of this band decreased with time as the catalyst became partial deactivated in ESR. Moreover, Montero et al. [46] found that non-filamentous coke (i.e., the condensed coke) was evolved on the deactivated catalyst at the late stage of ESR. The simultaneous increase of fractions of bands at ~1575 cm⁻¹ (C=C) and ~1444 cm⁻¹ (O=C–O assigned to acetate groups) indicated the contribution of accumulated acetate groups to the formation of the condensed coke. As presented in Figure 12b, the spent Ni/LiAlO₂@6Cu_6Ni after being used in the 5-h reaction of ESR shows that the C–O bonds still account for a high fraction (~44.7%) in the filamentous-like coke formation (the coke as shown in the TEM image in Figure 11d). Accordingly, the Ni/LiAlO₂@6Cu_6Ni catalyst could effectively decompose acetaldehyde, and this process is stable over time with a bare accumulation of acetate groups. The Cu/LiAlO₂@6Cu_6Ni first contacting to the ethanol-water mixture steam can initially dehydrogenate ethanol to form acetaldehyde; thus, the subsequent Ni/LiAlO₂@6Cu_6Ni could have high efficiency to decompose the acetaldehyde to generate H₂ and C1 gases directly. This process is stable over time, and it reduces the chance of acetaldehyde being oxidized by lattice oxygen or hydroxyl groups (–OH) on Ni/LiAlO₂ surface to form acetate acetic acid [12], which was found on spent Ni/LiAlO₂@6Ni. Through the pre-reaction of the ethanol-water mixture steam with the Cu/LiAlO₂@6Cu_6Ni, the Ni/LiAlO₂@6Cu_6Ni catalyst avoids the formation of condensed carbon.

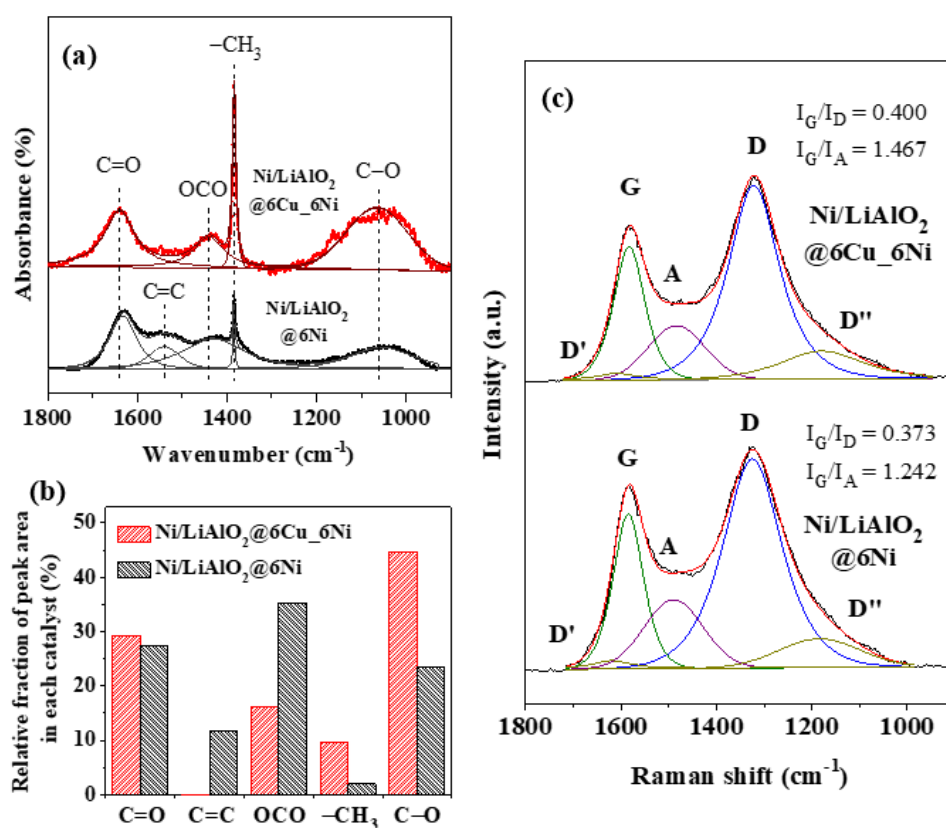


Figure 12. (a) FTIR spectra; (b) the relative fractions of peak area of the absorbance bands in each FTIR spectrum; (c) Raman spectra of the coke on spent Ni/LiAlO₂@6Cu_6Ni and Ni/LiAlO₂@6Ni catalysts that were used in the 5-h reactions of ESR. Reaction conditions: same as that described in Figure 10.

Figure 12c presents first-order Raman spectra of carbon from 900 to 1800 cm⁻¹. Two main characteristic peaks at around 1585 and 1310 cm⁻¹ (G and D in Figure 12c) in each spectrum respectively present the so-called G-band and D-band. The G-band is associated with stretching of the carbon sp² bonds in the ordered graphite structure, while the D-band arises from disordered carbon. As the ordered graphite begins to amorphize, a band that is associated with amorphous carbon appears at 1520 cm⁻¹ (the so-called A-band, indicated by A in Figure 12c) [48]. The other two relatively weak peaks at 1200 and 1620 cm⁻¹ are also associated with disordered carbon (D' and D'' in Figure 12c). Both of the Raman spectra in Figure 12c reveal the dominance of disordered carbon. To evaluate the degree of ordering of carbon, the peak areas of bands G, A, and D (represented by I_G, I_A, and I_D) are compared. The ratios I_G/I_D and I_G/I_A are indicated in Figure 12c. The carbon formation on the spent Ni/LiAlO₂@6Cu_6Ni had higher values of I_G/I_D (by ~7%) and I_G/I_A (by ~15%) ratios than those of the spent Ni/LiAlO₂@6Ni. The analysis by Raman spectroscopy confirms that the filamentous carbon forming on the spent Ni/LiAlO₂@6Cu_6Ni is more ordered and graphitized than the condensed coke formed on the spent Ni/LiAlO₂@6Ni. Figure S6 exhibits XRD patterns of the spent Ni/LiAlO₂@6Ni and Ni/LiAlO₂@6Cu_6Ni catalysts that were used in the 5-h reactions. The spent Ni/LiAlO₂@6Cu_6Ni (bottom pattern in Figure S6) yielded a broad peak at 26.4°, representing graphite (002). As for the spent Ni/LiAlO₂@6Ni (bottom pattern in Figure S6), this characteristic peak (at ~26°) could hardly be found. It exhibited large background signals at 2θ < 20°. The large background signals are considered to arise from their amorphous nature [46]. The XRD results agree with the crystallinity of carbon determined by Raman spectroscopy.

Temperature programmed oxidation (TPO) analysis was performed for the spent Ni/LiAlO₂@6Ni and Ni/LiAlO₂@6Cu_6Ni catalysts. As shown in Figure 13, both samples

start to consume oxygen at ~ 300 °C. The TPO data curve in black represented the oxygen consumption of the spent Ni/LiAlO₂@6Ni, presenting a oxygen combustion peak with maximum intensity at ~ 628 °C. The red curve plots the TPO data of the coke on spent Ni/LiAlO₂@6Cu_6Ni, showing a intensive oxygen combustion peak with a much wider full width at half maximum than that of the black peak, and the maximum oxygen consumption occurred at ~ 656 °C. Literature suggests that amorphous carbon burns in the air at 200–500 °C; the carbon with defects burns in the air between 500 and 600 °C; the graphitic carbon burns above 600 °C [49,50]. According to Figure 13, the TPO of the coke on spent Ni/LiAlO₂@6Cu_6Ni indicates a relatively high amount of graphitic carbon. This is related to the higher degree of ordering of coke on the spent Ni/LiAlO₂@6Cu_6Ni than that on the spent Ni/LiAlO₂@6Ni, which was also revealed by Raman spectroscopy (Figure 12c). Based on the area under the curve in Figure 13, the spent Ni/LiAlO₂@6Cu_6Ni consumes $\sim 48\%$ more oxygen than the spent Ni/LiAlO₂@6Ni by both using the same weight of the TPO samples. This indicates that the coke on spent Ni/LiAlO₂@6Cu_6Ni is highly composed of C with low content of O and H, which means it has to be burned at relatively high temperatures.

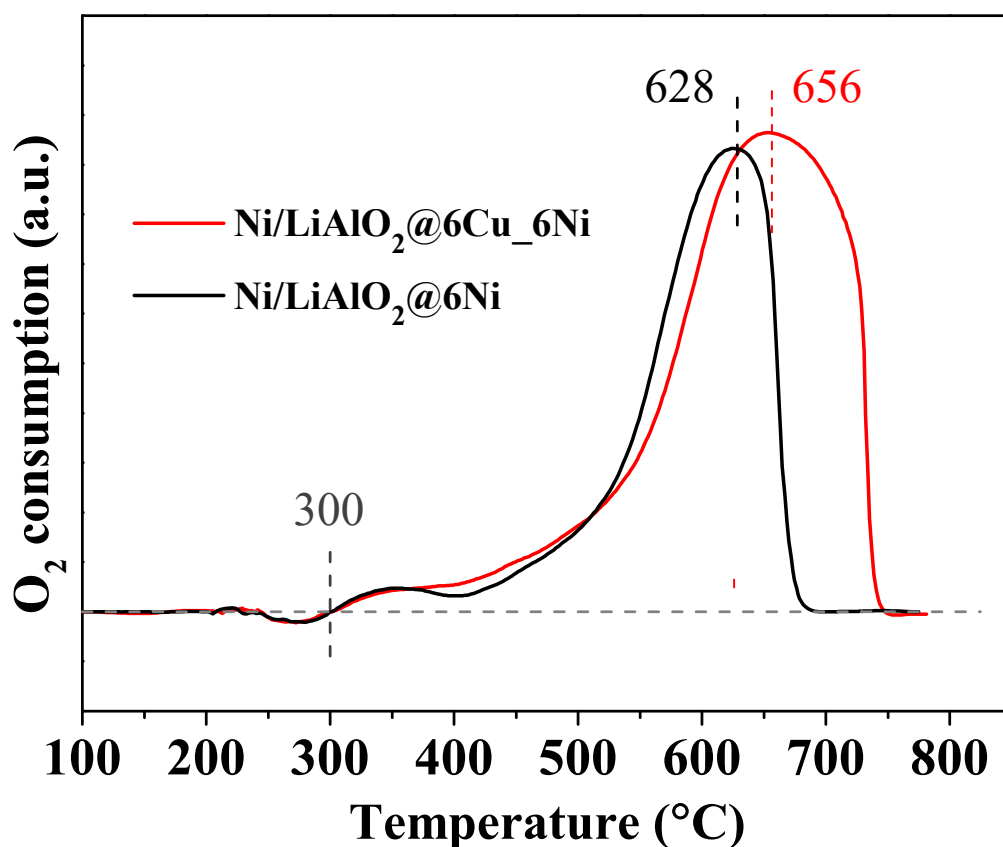


Figure 13. TPO profiles of the spent Ni/LiAlO₂@6Ni and Ni/LiAlO₂@6Cu_6Ni catalysts that had been tested after 5-h reactions of ESR. Reaction conditions: the same as that described in Figure 10.

3. Materials and Methods

3.1. Catalyst Preparation

Aluminum lathe strips were formed into cylindrical strip balls, working as a structural framework, with a diameter of about 4 cm and a length of about 4 cm, as shown in the photograph in Figure 14. The lathe strip ball (working as a framework structure to support the catalyst that would be formed on it afterward (see Figure S1)) was ultrasonically cleaned in acetone to remove the oil and debris from its surface. Al³⁺- and Li⁺-containing electrolyte solution was prepared by adding aluminum foil into a 0.06 M LiOH aqueous solution with a Li/Al molar ratio of two. To prepare the electrolyte solution, an appropriate amount

of $\text{LiOH}\cdot\text{H}_2\text{O}$ was dissolved in deionized water at $50\text{ }^\circ\text{C}$. The water was simultaneously purged with high-purity Ar gas to reduce any potential dissolution of contaminating CO_2 . Aluminum foil was cut into strips ($1\text{ mm} \times 5\text{ mm}$) and added to the aqueous LiOH solution. This solution was magnetically stirred for 30 min at $50\text{ }^\circ\text{C}$ and then filtered through a filter paper to obtain a clear solution, which was used as the electrolyte solution. A potentiostat (EG & G model 273A, Princeton Applied Research, US) in which the anode was platinum-coated titanium mesh and the cathode was the aluminum lathe strip ball (Figure 14) was used. The setup was used for electrodeposition for 2 h at a constant DC voltage of 5 V. The lathe waste strip ball that was coated with Li-Al-CO_3 LDH was then rinsed with distilled water.

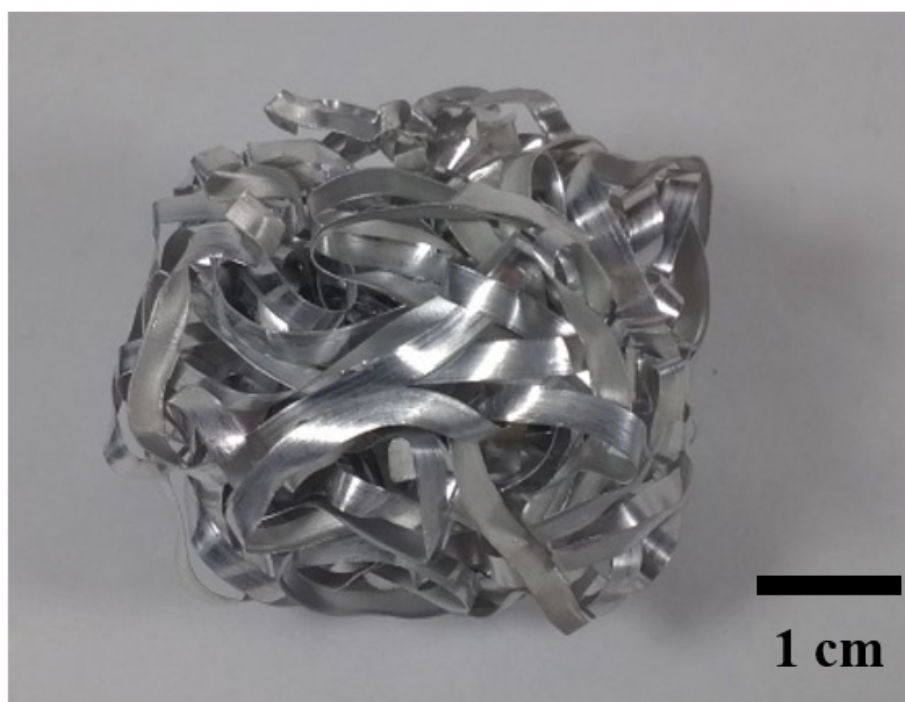


Figure 14. The photograph of the aluminum lathe waste strip ball working as a structured framework (this picture showing the framework before LDH and catalyst depositions), which would be employed as the substrate of the structured catalyst.

The LDH-coated aluminum lathe waste strip ball was calcined at $500\text{ }^\circ\text{C}$ for 1 h to increase the hydrophilicity of its surface. Appropriate amounts of $\text{NiCl}_2\cdot 6\text{H}_2\text{O}$ and $\text{CuCl}_2\cdot 2\text{H}_2\text{O}$ were respectively added into a magnetically stirred deionized water at $50\text{ }^\circ\text{C}$ to prepare 0.15 M Ni^{2+} - and 0.0012 M Cu^{2+} -containing aqueous solutions. Then, saturated aqueous NaHCO_3 was added dropwise to a pH value of 6.7 for the Ni^{2+} - and 7.5 for the Cu^{2+} -containing solution, respectively. The calcined LDH-coated lathe strip ball was immersed in the magnetically stirred Ni^{2+} - or Cu^{2+} -containing solutions for 1 h (see the immersion in Figure S1) to have Ni or Cu hydroxide precursor on it. The sample was then reduced with pure H_2 flow at $500\text{ }^\circ\text{C}$ in a tube furnace to complete the reduction reaction changing Ni/Cu hydroxide precursor into metallic Ni or Cu. The reduced catalysts were denoted as Ni/ LiAlO_2 and Cu/ LiAlO_2 , respectively.

3.2. Catalytic Tests

ESR tests were performed in a stainless-steel tubular reactor (6 cm in diameter and 45 cm long) at ambient pressure. The reactor consisted of two chambers: the first was used to heat and vaporize the feed ethanol solution. The vaporized gas was subsequently going into the second reactor where the catalysts explored herein were loaded into. These two chambers were preheated to $250\text{ }^\circ\text{C}$ and $500\text{ }^\circ\text{C}$, respectively, with hot N_2 gas flow as the

carrying gas herein. After the specified temperatures were reached, aqueous ethanol was fed into the first reactor by a diaphragm metering pump (KNF SIMDOWS 02). The outlet products out of the second reactor were cooled and then dried. The total gas flow rate was then measured using a flow meter and the gas phase was analyzed using an on-line gas analyzer. The contents of ethanol, acetaldehyde (in the liquid phase products), and ethylene (in the gas phase products) were determined using a gas chromatograph (GC, Agilent 7890CB). The column of RT-Q-BOND was equipped on GC to separate CO₂, CH₄, and other C-containing compounds from O₂, N₂, and CO, using He as the carrier gas. Ethanol conversion (X_{EtOH}) was estimated as follows.

$$X_{EtOH} = 1 - \frac{n_{EtOH}}{n_{EtOH,0}}, \quad (8)$$

where n_{EtOH} is the molar flow rate of ethanol in exhausted liquid and $n_{EtOH,0}$ is the molar feed rate of ethanol at the inlet. The yield (Y_i) of the output gas was calculated as follows.

$$Y_i = \frac{n_i}{v_i \times n_{EtOH,0}}, \quad (9)$$

where n_i is the molar flow rate of each gas at the outlet and v_i is the corresponding stoichiometric coefficient. The cumulative H₂ output was estimated by integrating n_{H_2} over time. In each ESR test, six of the lathe strip balls with the catalyst of Ni/LiAlO₂ catalyst or Cu/LiAlO₂ catalyst were used for testing (denoted as 6Ni and 6Cu, respectively). The catalyst configuration in which six lathe strip balls of Cu/LiAlO₂ catalyst were placed in front of six lathe strip balls of Ni/LiAlO₂ catalyst in the reaction chamber for the ESR test was denoted as 6Cu_6Ni. The total mass of the catalyst (LiAlO₂ support + catalyst particles) on six lathe strip balls of Ni/LiAlO₂ catalyst (6Ni) was 0.33 g and that on six lathe strip balls of Cu/LiAlO₂ catalyst (6Cu) was 0.28 g.

3.3. Material Characterization

The crystallographic structures of the as-prepared and used catalysts were determined by glancing angle X-ray diffraction (GAXRD, Bruker D8 Advance ECO) with a glancing angle of 0.5° using Cu Kα₁ (1.5406 Å) radiation. A field emission scanning electron microscope (FE-SEM, ZEISS Ultra Plus) was used to observe the surface morphologies of the as-prepared and used catalysts. X-ray photoelectron spectroscopy (XPS, ULVAC-PHI, PHI 5000 VersaProbe) was used to confirm the states of the surface elements. For the XPS study, the surface underwent Ar ion bombardment for 6 s to remove the surface-adsorbed gas, and surface data were then collected. The cross-sectional microstructures of the catalysts were determined and their phases were identified from their diffraction patterns that were collected using a field emission transmission electron microscope (FE-TEM, FEI Tecnai G2 F20). Specimens for TEM observation were prepared using a focused ion beam (FIB, Hitachi NX2000). A carbon film was deposited before FIB bombardment to protect the surface of the sample from damage.

CO₂ and NH₃ temperature programmed desorption (TPD) of the calcined LDH sample (the Li–Al LDH that was calcined at 500 °C for 3 h) was investigated by using a volumetric gas adsorption analyzer (Anton Paar Novatouch LX2, Austria). A total of 150 mg of the calcined LDH sample was used in each test. Prior to the TPD test, the adsorption of CO₂ was performed at 100 °C for 1 h by flowing a 15% CO₂/N₂ gas mixture passing through the sample. Followed by flushing the sample with He at room temperature for 1 h for removing any physically adsorbed CO₂. TPD of CO₂ was carried out at a heating rate of 10 °C/min from the room temperature to 600 °C. NH₃ adsorption was performed at 30 °C for 1 h by using a 15% NH₃/N₂ flow, and then flushed with He at room temperature for 1 h for removing any physically adsorbed NH₃. TPD of NH₃ was carried out at a heating rate of 20 °C/min from the room temperature to 600 °C.

The powder of coke dropped from the catalysts was collected for the characterization of the coke formation. Fourier transform infrared (FTIR) spectra were obtained

using a Perkin-Elmer Spectrum 65 FT-IR spectrometer over the range of wavenumber of 900–1800 cm^{-1} with a resolution of 4 cm^{-1} , using the KBr pressed disc method. The crystallinity degree of the coke was determined by Raman spectroscopy (Tokyo Instruments, Nanofinder 30) with a 632.8 nm He-Ne laser source. Before FTIR, each sample was dried in an oven to remove H_2O molecular from sample's surface. Temperature programmed oxidation (TPO) was carried out using a volumetric gas adsorption analyzer (Anton Paar Novatouch LX2, Austria). The coke sample (10 mg) was first flushed with an N_2 flow at 100 °C, then subsequently an airflow was introduced, heating up to 800 °C at 5 °C/min. The consumption signals of oxygen were simultaneously recorded.

4. Conclusions

A process of recovering metal ions from simulated Ni or Cu electroplating wastewater for use in synthesizing nano-catalysts was proposed. A coating of Li–Al layered double hydroxide (LDH) with nano-sized platelet structure was successfully electrodeposited on the surface of aluminum lathe waste. The LDH works as catalyst support with a high surface area for being loaded with many catalytic nanoparticles. The calcined Li–Al LDH, owing to good hydrophilicity, can adsorb ions of Ni or Cu during dipping in the aqueous solution containing ions of Ni or Cu. It can be regarded as irreversible fouling of precursors such as Ni or Cu hydrate hydroxides on the surface of platelets, possibly owing to the concentration of solute on the surface of platelets exceeding the solubility product. By the reduction treatment with H_2 at 500 °C, Ni- or Cu-based nanoparticles can be formed on the surface of LiAlO_2 (derived from Li–Al LDH) platelets. LiAlO_2 , as for the catalyst support, exhibits high basicity, which is conducive to the initial adsorption of ethanol on its surface. The introduction of metal nanoparticles onto LiAlO_2 platelets (the Cu/ LiAlO_2 and Ni/ LiAlO_2 catalysts) had combined advantages of easy absorption of ethanol molecules on LiAlO_2 surface and the enhancement of ethanol dehydrogenation and acetaldehyde conversion reactions by the metal catalysts. The use of aluminum lathe waste to prepare the structured catalyst eliminates the requirement of background pressure in ESR, making the reaction to perform effectively under ambient pressure. The Cu–Ni two-stage catalyst configuration (6Cu_6Ni) increased the H_2 production rate by about 10% compared with the only Ni-based catalyst configuration (6Ni). It also improves the stability of H_2 output in the 5-h reaction of ESR compared with 6Ni. The gas produced by using 6Cu_6Ni at 500 °C contains a lower CO concentration (less than 1%) compared with previous studies that applied Ni–Cu bimetal catalysts to ESR (mostly more than 2%), which is advantageous for its application. Coke formation on the spent Ni/ LiAlO_2 catalyst in 6Cu_6Ni was in the form of relatively graphitized carbon filaments, which did not significantly deactivate the catalyst. The pre-reaction of ethanol–water mixture steam with Cu catalyst in ESR provides a way to improve Ni catalyst's catalytic efficiency and stability. The pre-reaction reduces the partial deactivation behavior of the Ni catalyst and the sintering of the Ni nanoparticles.

Supplementary Materials: The following are available online at <https://www.mdpi.com/article/10.3390/catal11091124/s1>, Figure S1: Recovering of Ni^{2+} (a) and Cu^{2+} (b) from the simulated wastewater were found, with the changes of the concentrations of (a) Ni^{2+} from 535 ppm to 3.3 ppm between the initial and after the immersion time of 9 h (by using three calcined LDH-coated frameworks consecutively, each was dipped for 3 h); (b) Cu^{2+} decreased from 78 ppm to 4.8 ppm between the initial time and the immersion time of 1 h. The concentration of the cations in the solutions was measured by an inductively coupled plasma optical emission spectrometer (ICP-OES, US, Agilent 5110 ICP-OES), Figure S2: GC-MS results of gas-phase products for ESR over catalyst configurations which generate abundant gas (i.e., 6Ni and 6Cu_6Ni) at a reaction time of 1 h compared with air atmosphere. NL means the normalization level. Reaction conditions: same as that described in Figure 7, Figure S3: (a) GC-MS results of condensed liquid phase products for ESR over various catalyst configurations at a reaction time of 1 h compared with H_2O ; (b) magnification view of the peaks corresponding to acetaldehyde. NL means the normalization level. Reaction conditions: same as that described in Figure 7, Figure S4: (a) XRD pattern; (b) SEM surface morphology of the spent Cu/ LiAlO_2 @6Cu_6Ni catalyst that was used in 5-h reaction of ESR. Reaction conditions: same

as that described in Figure 10, Figure S5: Selected area diffraction patterns of the particles on the spent catalysts that were used in 5-h reactions of ESR: (a) Ni/LiAlO₂@6Ni; (b) Ni/LiAlO₂@6Cu₆Ni. Reaction conditions: same as that described in Figure 10, Figure S6: GAXRD patterns of the spent Ni/LiAlO₂@6Ni and Ni/LiAlO₂@6Cu₆Ni catalysts that were used in 5-h reactions of ESR. Reaction conditions: same as that described in Figure 10.

Author Contributions: Conceptualization, J.-Y.U.; methodology, Y.-J.C.; validation, S.-H.H.; investigation, Y.-J.C.; data curation, Y.-J.C.; writing—original draft preparation, J.-Y.U.; writing—review and editing, Y.-J.C.; visualization, Y.-J.C.; supervision, J.-Y.U.; project administration, H.-T.L.; funding acquisition, H.-T.L. All authors have read and agreed to the published version of the manuscript.

Funding: This research was funded by Bureau of Energy, Grant No.110-E0202.

Data Availability Statement: The data that support the findings of this study are available on request from the corresponding author. The data are not publicly available due to privacy or ethical restrictions.

Acknowledgments: The financial support provided by Bureau of Energy (Grant No.110-E0202) is gratefully acknowledged.

Conflicts of Interest: The authors declare no conflict of interest.

References

1. Castelblanque, J.; Salimbeni, F. NF and RO membranes for the recovery and reuse of water and concentrated metallic salts from waste water produced in the electroplating process. *Desalination* **2004**, *167*, 65–73. [[CrossRef](#)]
2. Al-Shannag, M.; Al-Qodah, Z.; Bani-Melhem, K.; Qtaishat, M.R.; Alkasrawi, M. Heavy metal ions removal from metal plating wastewater using electrocoagulation: Kinetic study and process performance. *Chem. Eng. J.* **2015**, *260*, 749–756. [[CrossRef](#)]
3. Buxton, S.; Garman, E.; Heim, K.E.; Lyons-Darden, T.; Schlekot, C.E.; Taylor, M.D.; Oller, A.R. Concise review of nickel human health toxicology and ecotoxicology. *Inorganics* **2019**, *7*, 89. [[CrossRef](#)]
4. Chang, Y.C.; Uan, J.Y. Mg₁₇Al₁₂ phase in magnesium alloy waste facilitating the Ni²⁺ reduction in nickel plating wastewater. *J. Hazard. Mater.* **2021**, *403*, 123556. [[CrossRef](#)]
5. Acar, C.; Dincer, I. Comparative assessment of hydrogen production methods from renewable and non-renewable sources. *Int. J. Hydrogen Energy* **2014**, *39*, 1–12. [[CrossRef](#)]
6. Liao, C.H.; Huang, C.W.; Wu, J. Hydrogen production from semiconductor-based photocatalysis via water splitting. *Catalysts* **2012**, *2*, 490–516. [[CrossRef](#)]
7. Sapountzi, F.M.; Gracia, J.M.; Fredriksson, H.O.; Niemantsverdriet, J.H. Electrocatalysts for the generation of hydrogen, oxygen and synthesis gas. *Prog. Energy Combust. Sci.* **2017**, *58*, 1–35. [[CrossRef](#)]
8. Yu, S.H.; Uan, J.Y.; Hsu, T.L. Effects of concentrations of NaCl and organic acid on generation of hydrogen from magnesium metal scrap. *Int. J. Hydrogen Energy* **2012**, *37*, 3033–3040. [[CrossRef](#)]
9. Hosseini, S.E.; Abdul Wahid, M.; Jamil, M.; Azli, A.A.; Misbah, M.F. A review on biomass-based hydrogen production for renewable energy supply. *Int. J. Energy Res.* **2015**, *39*, 1597–1615. [[CrossRef](#)]
10. Konsolakis, M.; Ioakimidis, Z.; Kraia, T.; Marnellos, G.E. Hydrogen production by ethanol steam reforming (ESR) over CeO₂ supported transition metal (Fe, Co, Ni, Cu) catalysts: Insight into the structure-activity relationship. *Catalysts* **2016**, *6*, 39. [[CrossRef](#)]
11. Hou, T.; Zhang, S.; Chen, Y.; Wang, D.; Cai, W. Hydrogen production from ethanol reforming: Catalysts and reaction mechanism. *Renew. Sustain. Energy Rev.* **2015**, *44*, 132–148. [[CrossRef](#)]
12. Li, D.; Li, X.; Gong, J. Catalytic reforming of oxygenates: State of the art and future prospects. *Chem. Rev.* **2016**, *116*, 11529–11653. [[CrossRef](#)] [[PubMed](#)]
13. Freni, S.; Mondello, N.; Cavallaro, S.; Cacciola, G.; Parmon, V.; Sobyanin, V. Hydrogen production by steam reforming of ethanol: A two step process. *React. Kinet. Catal. Lett.* **2000**, *71*, 143–152. [[CrossRef](#)]
14. Sikander, U.; Sufian, S.; Salam, M. A review of hydrotalcite based catalysts for hydrogen production systems. *Int. J. Hydrogen Energy* **2017**, *42*, 19851–19868. [[CrossRef](#)]
15. Syu, J.H.; Uan, J.Y.; Lin, M.C.; Lin, Z.Y. Optically transparent Li–Al–CO₃ layered double hydroxide thin films on an AZ31 Mg alloy formed by electrochemical deposition and their corrosion resistance in a dilute chloride environment. *Corros. Sci.* **2013**, *68*, 238–248. [[CrossRef](#)]
16. Lin, M.C.; Chang, F.T.; Uan, J.Y. Aqueous Li⁺/Al³⁺ alkaline solution for CO₂ capture and the massive Li–Al–CO₃ hydrotalcite precipitation during the interaction between CO₂ gas and the Li⁺/Al³⁺ aqueous solution. *J. Mater. Chem. A.* **2013**, *1*, 14773–14782. [[CrossRef](#)]
17. Huang, S.H.; Liu, S.J.; Uan, J.Y. Controllable luminescence of a Li–Al layered double hydroxide used as a sensor for reversible sensing of carbonate. *J. Mater. Chem. C.* **2019**, *7*, 11191–11206. [[CrossRef](#)]

18. Stepanova, L.; Belskaya, O.; Vasilevich, A.; Gulyaeva, T.; Leont'eva, N.; Serkova, A.; Salanov, A.; Likholobov, V. The study of structural, textural and basic properties of MgAl- and LiAl-LDH prepared by mechanochemical method. *Catal. Today* **2019**. [[CrossRef](#)]
19. Di Cosimo, J.; Díez, V.; Xu, M.; Iglesia, E.; Apestegua, C. Structure and surface and catalytic properties of Mg-Al basic oxides. *J. Catal.* **1998**, *178*, 499–510. [[CrossRef](#)]
20. Cybulski, A.; Moulijn, J.A. *Structured Catalysts and Reactors*; CRC Press: Boca Raton, FL, USA, 2005.
21. López, E.; Divins, N.J.; Anzola, A.; Schbib, S.; Borio, D.; Llorca, J. Ethanol steam reforming for hydrogen generation over structured catalysts. *Int. J. Hydrogen Energy* **2013**, *38*, 4418–4428. [[CrossRef](#)]
22. Palma, V.; Ruocco, C.; Castaldo, F.; Ricca, A.; Boettge, D. Ethanol steam reforming over bimetallic coated ceramic foams: Effect of reactor configuration and catalytic support. *Int. J. Hydrogen Energy* **2015**, *40*, 12650–12662. [[CrossRef](#)]
23. Santander, J.A.; Tonetto, G.M.; Pedernera, M.N.; López, E. Ni/CeO₂-MgO catalysts supported on stainless steel plates for ethanol steam reforming. *Int. J. Hydrogen Energy* **2017**, *42*, 9482–9492. [[CrossRef](#)]
24. Palma, V.; Gallucci, F.; Pullumbi, P.; Ruocco, C.; Meloni, E.; Martino, M. Pt/Re/CeO₂ Based Catalysts for CO-Water-Gas Shift Reaction: From Powders to Structured Catalyst. *Catalysts* **2020**, *10*, 564. [[CrossRef](#)]
25. Wang, S.L.; Lin, C.H.; Yan, Y.Y.; Wang, M.K. Synthesis of Li/Al LDH using aluminum and LiOH. *Appl. Clay Sci.* **2013**, *72*, 191–195. [[CrossRef](#)]
26. Liang, X.; Zang, Y.; Xu, Y.; Tan, X.; Hou, W.; Wang, L.; Sun, Y. Sorption of metal cations on layered double hydroxides. *Colloids Surf. A* **2013**, *433*, 122–131. [[CrossRef](#)]
27. Huang, L.; Wang, J.; Gao, Y.; Qiao, Y.; Zheng, Q.; Guo, Z.; Zhao, Y.; O'Hare, D.; Wang, Q. Synthesis of LiAl₂-layered double hydroxides for CO₂ capture over a wide temperature range. *J. Mater. Chem. A* **2014**, *2*, 18454–18462. [[CrossRef](#)]
28. Choong, C.K.; Huang, L.; Zhong, Z.; Lin, J.; Hong, L.; Chen, L. Effect of calcium addition on catalytic ethanol steam reforming of Ni/Al₂O₃: II. Acidity/basicity, water adsorption and catalytic activity. *Appl. Catal. A* **2011**, *407*, 155–162. [[CrossRef](#)]
29. Li, Z.; Hu, X.; Zhang, L.; Liu, S.; Lu, G. Steam reforming of acetic acid over Ni/ZrO₂ catalysts: Effects of nickel loading and particle size on product distribution and coke formation. *Appl. Catal. A* **2012**, *417*, 281–289. [[CrossRef](#)]
30. Meng, F.; Li, X.; Li, M.; Cui, X.; Li, Z. Catalytic performance of CO methanation over La-promoted Ni/Al₂O₃ catalyst in a slurry-bed reactor. *Chem. Eng. J.* **2017**, *313*, 1548–1555. [[CrossRef](#)]
31. Chen, G.; Tao, J.; Liu, C.; Yan, B.; Li, W.; Li, X. Steam reforming of acetic acid using Ni/Al₂O₃ catalyst: Influence of crystalline phase of Al₂O₃ support. *Int. J. Hydrogen Energy* **2017**, *42*, 20729–20738. [[CrossRef](#)]
32. Chen, L.C.; Lin, S.D. The ethanol steam reforming over Cu-Ni/SiO₂ catalysts: Effect of Cu/Ni ratio. *Appl. Catal. B* **2011**, *106*, 639–649. [[CrossRef](#)]
33. Knapp, R.; Wyrzgol, S.A.; Jentys, A.; Lercher, J.A. Water-gas shift catalysts based on ionic liquid mediated supported Cu nanoparticles. *J. Catal.* **2010**, *276*, 280–291. [[CrossRef](#)]
34. Wang, Z.Q.; Xu, Z.N.; Peng, S.Y.; Zhang, M.J.; Lu, G.; Chen, Q.S.; Chen, Y.; Guo, G.C. High-performance and long-lived Cu/SiO₂ nanocatalyst for CO₂ hydrogenation. *ACS Catal.* **2015**, *5*, 4255–4259. [[CrossRef](#)]
35. Zhang, X.; Zhu, X.; Lin, L.; Yao, S.; Zhang, M.; Liu, X.; Wang, X.; Li, Y.-W.; Shi, C.; Ma, D. Highly dispersed copper over β-Mo₂C as an efficient and stable catalyst for the reverse water gas shift (RWGS) reaction. *ACS Catal.* **2017**, *7*, 912–918. [[CrossRef](#)]
36. Lee, C.H.; Kim, S.; Yoon, H.J.; Yoon, C.W.; Lee, K.B. Water gas shift and sorption-enhanced water gas shift reactions using hydrothermally synthesized novel Cu-Mg-Al hydrotalcite-based catalysts for hydrogen production. *Renew. Sust. Energ. Rev.* **2021**, *145*, 111064. [[CrossRef](#)]
37. Marks, K.; Besharat, Z.; Soldemo, M.; Önstén, A.; Weissenrieder, J.; Stenlid, J.H.; Öström, H.; Göthelid, M. Adsorption and Decomposition of Ethanol on Cu₂O (111) and (100). *J. Phys. Chem. C* **2019**, *123*, 20384–20392. [[CrossRef](#)]
38. Sato, A.G.; Volanti, D.P.; de Freitas, I.C.; Longo, E.; Bueno, J.M.C. Site-selective ethanol conversion over supported copper catalysts. *Catal. Commun.* **2012**, *26*, 122–126. [[CrossRef](#)]
39. Cunha, A.F.; Wu, Y.-J.; Li, P.; Yu, J.-G.; Rodrigues, A.E. Sorption-enhanced steam reforming of ethanol on a novel K-Ni-Cu-hydrotalcite hybrid material. *Ind. Eng. Chem. Res.* **2014**, *53*, 3842–3853. [[CrossRef](#)]
40. Chen, F.; Tao, Y.; Ling, H.; Zhou, C.; Liu, Z.; Huang, J.; Yu, A. Ni-Cu bimetallic catalysts on Ytria-stabilized zirconia for hydrogen production from ethanol steam reforming. *Fuel* **2020**, *280*, 118612. [[CrossRef](#)]
41. Dai, R.; Zheng, Z.; Lian, C.; Shi, K.; Wu, X.; An, X.; Xie, X. A sinter-resistant catalytic system based on ultra-small Ni-Cu nanoparticles encapsulated in Ca-SiO₂ for high-performance ethanol steam reforming. *Nanoscale* **2020**, *12*, 16605–16616. [[CrossRef](#)]
42. Niazi, Z.; Irankhah, A.; Wang, Y.; Arandiyán, H. Cu, Mg and Co effect on nickel-ceria supported catalysts for ethanol steam reforming reaction. *Int. J. Hydrogen Energy* **2020**, *45*, 21512–21522. [[CrossRef](#)]
43. Zheng, Z.; Sun, C.; Dai, R.; Wang, S.; Wu, X.; An, X.; Wu, Z.; Xie, X. Ethanol steam reforming on Ni-based catalysts: Effect of Cu and Fe addition on the catalytic activity and resistance to deactivation. *Energy Fuels* **2017**, *31*, 3091–3100. [[CrossRef](#)]
44. Devrim, Y.; Albostan, A.; Devrim, H. Experimental investigation of CO tolerance in high temperature PEM fuel cells. *Int. J. Hydrogen Energy* **2018**, *43*, 18672–18681. [[CrossRef](#)]
45. Ochoa, A.; Aramburu, B.; Ibáñez, M.; Valle, B.; Bilbao, J.; Gayubo, A.G.; Castaño, P. Compositional insights and valorization pathways for carbonaceous material deposited during bio-oil thermal treatment. *ChemSusChem* **2014**, *7*, 2597–2608. [[CrossRef](#)] [[PubMed](#)]

46. Montero, C.; Ochoa, A.; Castaño, P.; Bilbao, J.; Gayubo, A.G. Monitoring Ni⁰ and coke evolution during the deactivation of a Ni/La₂O₃-αAl₂O₃ catalyst in ethanol steam reforming in a fluidized bed. *J. Catal.* **2015**, *331*, 181–192. [[CrossRef](#)]
47. Ochoa, A.; Arregi, A.; Amutio, M.; Gayubo, A.G.; Olazar, M.; Bilbao, J.; Castaño, P. Coking and sintering progress of a Ni supported catalyst in the steam reforming of biomass pyrolysis volatiles. *Appl. Catal. B* **2018**, *233*, 289–300. [[CrossRef](#)]
48. Merlen, A.; Buijnsters, J.G.; Pardanaud, C. A guide to and review of the use of multiwavelength Raman spectroscopy for characterizing defective aromatic carbon solids: From graphene to amorphous carbons. *Coatings* **2017**, *7*, 153. [[CrossRef](#)]
49. Velasquez, M.; Batiot-Dupeyrat, C.; Gallego, J.; Santamaria, A. Chemical and morphological characterization of multi-walled-carbon nanotubes synthesized by carbon deposition from an ethanol-glycerol blend. *Diam. Relat. Mater.* **2014**, *50*, 38–48. [[CrossRef](#)]
50. Charisiou, N.; Tzounis, L.; Sebastian, V.; Hinder, S.; Baker, M.; Polychronopoulou, K.; Goula, M. Investigating the correlation between deactivation and the carbon deposited on the surface of Ni/Al₂O₃ and Ni/La₂O₃-Al₂O₃ catalysts during the biogas reforming reaction. *Appl. Surf. Sci.* **2019**, *474*, 42–56. [[CrossRef](#)]